

Black Holes as Fermion Factories

Yifan Chen ^a, Xiao Xue ^{b,c,d}, and Vitor Cardoso ^{a,e}

^aNiels Bohr International Academy, Niels Bohr Institute, Blegdamsvej 17, 2100 Copenhagen, Denmark

^bInstitut de Física d'Altes Energies (IFAE), The Barcelona Institute of Science and Technology, Campus UAB, 08193 Bellaterra (Barcelona), Spain

^cII. Institute of Theoretical Physics, Universität Hamburg, 22761 Hamburg, Germany

^dDeutsches Elektronen-Synchrotron DESY, Notkestr. 85, 22607, Hamburg, Germany

^eCENTRA, Departamento de Física, Instituto Superior Técnico – IST, Universidade de Lisboa – UL, Avenida Rovisco Pais 1, 1049 Lisboa, Portugal

E-mail: yifan.chen@nbi.ku.dk, xxue@ifae.es, vitor.cardoso@nbi.ku.dk

Abstract. Ultralight bosons near rotating black holes can undergo significant growth through superradiant energy extraction, potentially reaching field values close to the Planck scale and transforming black holes into effective transducers for these fields. The interaction between boson fields and fermions may lead to parametric production or Schwinger pair production of fermions, with efficiencies significantly exceeding those of perturbative decay processes. Additionally, the spatial gradients of scalar clouds and the electric components of vector clouds can accelerate fermions, resulting in observable fluxes. This study considers both Standard Model neutrinos and dark sector fermions, which could contribute to boosted dark matter. Energy loss due to fermion emissions can potentially quench the exponential growth of the cloud, leading to a saturated state. This dynamic provides a framework for establishing limits on boson-neutrino interactions, previously constrained by neutrino self-interaction considerations. In the saturation phase, boson clouds have the capacity to accelerate fermions to TeV energies, producing fluxes that surpass those from atmospheric neutrinos near black holes. These fluxes open new avenues for observations through high-energy neutrino detectors like IceCube, as well as through dark matter direct detection efforts focused on targeted black holes.

Keywords: black hole, superradiance, ultralight boson, neutrino, boosted dark matter

Preprint numbers: DESY-23-109

Contents

1	Introduction	1
2	Fermion Production from Superradiant Clouds	3
2.1	Superradiance	3
2.2	Particle Production from Boson Condensates	4
2.2.1	Parametric Matter Production from Scalar Backgrounds	5
2.2.2	Schwinger Pair Production from Vector Backgrounds	6
2.2.3	Fermion Production from Boson Clouds	7
2.3	Fermion Acceleration and Resulting Fluxes from Boson Clouds	8
2.4	Saturating Cloud States	12
3	Spin Measurements for Neutrino-Boson Interaction	14
4	Neutrino and Boosted Dark Matter Fluxes from Superradiant Clouds	17
5	Discussion	17

1 Introduction

Hypothetical bosons with ultralight masses are promising candidates in the search for physics beyond the Standard Model. Their potential to explain phenomena such as the smallness of the neutron electric dipole moment [1–3] and their emergence from fundamental theories that incorporate extra dimensions [4–7] make them particularly intriguing. When these bosons form dark matter and possess masses below $\mathcal{O}(1)$ eV, they manifest as coherent waves due to their typically high occupation numbers [8]. The interactions between an ultralight boson background and Standard Model particles can generate observable signals, distinguished by their frequency and proportional to the energy density or field value of the bosons.

When the Compton wavelength of these bosons is comparable to the gravitational radius of a rapidly rotating black hole (BH), a bound state may form through the superradiance mechanism, which extracts rotational energy from the BH [9–14]. This leads to the condensation of a bosonic structure, known as a boson cloud, in the exterior of the BH [11–13]. These superradiant clouds can amass up to approximately 10% of the BH mass [15–17], reaching field values near the grand unification theory (GUT) scale [18], significantly surpassing the local dark matter field value. Thus, Kerr BHs can serve as potent transducers for ultralight bosons [14]. The detection of superradiant phenomena does not require that ultralight bosons constitute the majority of dark matter and can be achieved through various methods, including BH spin-down [15, 19–28], gravitational wave signals from boson clouds [18–22, 25, 29–42], and axion cloud-induced birefringence [43–46].

For a boson field with minimal gravitational interaction, the exponential superradiant growth persists until the BH spin reaches the threshold for spin-down, with the cloud mass growing to approximately 10% of the BH mass. Afterward, the cloud slowly decays via gravitational wave emission. As a result, BH spin measurements and gravitational wave

detections from the cloud are the two primary observables for probing ultralight bosons with masses satisfying the superradiance condition.

On the other hand, boson self-interactions and interactions with other fields can potentially transform the bound state of the cloud into fluxes escaping to infinity, thereby quenching the exponential growth. When the energy leakage rate becomes comparable to the superradiant energy gain rate from the BH, the cloud enters a quasi-equilibrium state. Previous studies have demonstrated that both axion self-interactions [19, 29, 47–55] and axion-photon couplings [56–59] can lead to a saturation phase following the exponential growth stage.

Studying the potential interactions involving ultralight bosons is therefore crucial for understanding the superradiance mechanism. These interactions can terminate exponential growth before significant backreaction on the BH spin occurs, potentially making BH spin-down negligible and gravitational wave emission inefficient. Detailed calculations of energy emission rates and the saturation cloud mass are required to determine the exclusion region for interaction strengths, which typically exclude sufficiently weak couplings. Furthermore, the total cloud mass during saturation, a macroscopic quantity, is directly related to the microscopic interactions responsible for energy emission.

The particle production from a superradiant cloud can be significantly enhanced due to the GUT-scale field values near BHs, providing a unique testing ground for non-perturbative physics. Such particle production is traditionally studied in the context of early universe cosmology, where a dense, coherently oscillating scalar background induces parametric resonance, leading to enhanced matter production [60, 61]. A key difference between the superradiant cloud and the cosmological scalar background lies in the non-uniform spatial distribution of the cloud’s wavefunction. Additionally, in the realm of strong-field quantum electrodynamics, a strong electromagnetic field background is known to produce matter-antimatter pairs via the Schwinger pair production mechanism [62].

In this study, we demonstrate that both scalar and vector clouds surrounding BHs, by leveraging their significant field strengths, can produce substantial fermion fluxes through parametric excitation [60, 61] and Schwinger pair production [62], respectively. Furthermore, the non-uniform scalar cloud background and the electric components of the vector cloud can further accelerate the produced fermions, resulting in high-energy fluxes. A dark-sector fermion flux with velocities exceeding those of cold dark matter is commonly referred to as boosted dark matter, which can be probed by terrestrial dark matter and neutrino detectors [63–76].

We further consider the interaction between ultralight bosons and neutrinos. Among the various interactions between ultralight bosons and the Standard Model, the interaction with neutrinos is particularly well-motivated, primarily due to its implications for neutrino mass generation [77] and grand unification theories [78–80]. However, exploring these interactions poses significant challenges due to the difficulties in neutrino production and detection, with neutrino self-interaction being the primary observable [81]. Despite these challenges, when bosons meet the superradiance condition, their resulting neutrino fluxes from nearby BHs have the potential to surpass the ambient diffusive neutrino background [82], opening new possibilities for high-energy neutrino detection.

The structure of this paper is as follows: Section 2 details how scalar or vector clouds with significant field values can produce fermions more efficiently than perturbative decay and accelerate them to higher energies. This section also explores the possibility of reaching a saturation state where total fermion emissions balance the superradiant energy input from BHs. Section 3 examines how measurements of BH spins can exclude parameter spaces with

weak coupling strengths. Section 4 considers potential observational channels for detecting fermion fluxes in the viable parameter space. Section 5 summarizes the results and discusses prospects for future observations.

2 Fermion Production from Superradiant Clouds

This section begins with a brief introduction to superradiance, covering the superradiance conditions for both scalar and vector fields, the wavefunction of the superradiant ground state, and possible mechanisms to quench exponential growth. We then focus on matter production from boson condensates, including parametric production and Schwinger pair production of fermions. Next, we calculate and simulate the acceleration trajectories of these particles within the cloud, considering the non-uniformity of scalar clouds and the electric components of vector clouds. Finally, we discuss the potential saturation of the cloud state, resulting from the balance between the BH’s superradiant energy input and the emission of fermions.

2.1 Superradiance

Ultralight bosons, often predicted in theories incorporating extra dimensions [4–7], are promising candidates for cold dark matter [1–3, 83], notable for their wave-like properties [8]. These properties facilitate the formation of bound states known as gravitational atoms around BHs, resulting from gravitational attraction [11]. These states are characterized by unique quantum numbers and are influenced by the gravitational fine-structure constant, denoted as $\alpha \equiv G_{\text{N}}M_{\text{BH}}\mu$ [11, 14], where G_{N} is Newton’s constant, M_{BH} is the BH mass, and μ is the boson mass.

Around Kerr BHs, gravitational atoms with specific quantum numbers that corotate with the BH can undergo exponential growth by extracting energy through BH rotation, a phenomenon known as superradiance [9–14]. The parameter α must satisfy the superradiant condition formulated as:

$$\frac{\alpha}{m} < \frac{a_J}{2(1 + \sqrt{1 - a_J^2})}, \quad (2.1)$$

where a_J represents the BH’s dimensionless spin parameter, and m is the azimuthal quantum number of the gravitational atom, with $m > 0$ indicating corotation with the BH.

Since ground states in superradiance exhibit the fastest growth rates, our analysis focuses on these states. Under the Newtonian approximation ($\alpha \ll 1$), the wavefunctions for both scalar and vector fields are expressed as follows: [11, 14, 21, 84]

$$\begin{aligned} \phi &= \Psi_0(t) e^{1 - \alpha^2 r / (2r_g)} \frac{\alpha^2 r}{2r_g} \cos(\mu t - \varphi) \sin \theta, \\ A'^{\mu} &= \Psi_0(t) e^{-\alpha^2 r / r_g} (\alpha \sin \theta \sin(\mu t - \varphi), \cos(\mu t), \sin(\mu t), 0), \end{aligned} \quad (2.2)$$

utilizing Boyer-Lindquist coordinates (t, r, θ, φ) . Here, ϕ and A'^{μ} represent the scalar field and the components of the vector field in the unitary gauge, respectively. Ψ_0 denotes the peak field value within the bosonic cloud, and $r_g \equiv G_{\text{N}}M_{\text{BH}}$ represents the gravitational radius. The Newtonian approximation for these wavefunctions is valid in the region where $r \gg r_g$. Since the cloud size, or the Bohr radius, is on the order of r_g/α^2 , this approximation is appropriate in the regime of small α , where the majority of the cloud resides at distances

satisfying $r \gg r_g$. In this study, we consider $\alpha < 0.3$ to ensure that the condition for the Newtonian approximation is met.

The superradiant growth rate, Γ_{SR} , is approximated as $\alpha^8 a_J \mu / 24$ for scalar fields and $4\alpha^6 a_J \mu$ for vector fields when $\alpha \ll 1$ [11]. Notably, since the exponential growth is insensitive to the initial conditions, the detection of superradiant phenomena does not require that ultralight bosons constitute the majority of dark matter.

In cases where a boson minimally interacts with gravity, energy extraction from the BH rotation continues until the mass of the boson cloud, denoted as M_{cloud} , approximates about 10% of the BH mass [15–17]. Without an external influx of angular momentum, reaching this $10\%M_{\text{BH}}$ threshold causes the BH’s spin to decrease to a point where superradiance is no longer supported. Integrating the energy density of the cloud over its entire volume allows us to estimate the total mass of the cloud, $M_{\text{cloud}} \approx 186\Psi_0^2/(\alpha^3\mu)$ for scalar fields and $\pi\Psi_0^2/(\alpha^3\mu)$ for vector fields [18]. When M_{cloud} constitutes 10% of the BH mass, M_{BH} , the field values approach Planck scales:

$$\Psi_0 = \left(\frac{\alpha}{0.2}\right)^2 \left(\frac{M_{\text{cloud}}}{10\%M_{\text{BH}}}\right)^{1/2} \times \begin{cases} 1.1 \times 10^{16} \text{ GeV}, & \text{Scalar} \\ 8.7 \times 10^{16} \text{ GeV}. & \text{Vector} \end{cases} \quad (2.3)$$

Hereafter, we define $\Psi_0^{10\%}$ as the maximum permissible field value by setting $M_{\text{cloud}}/M_{\text{BH}} = 0.1$.

Exponential growth of superradiant clouds can be halted before causing significant back-reaction on the BH if there is an interaction between the boson cloud and other fields. In such scenarios, the cloud reaches a quasi-equilibrium state where these interactions induce a continuous outflow of energy. This outflow balances the energy gain from superradiance, maintaining an equilibrium state. Examples of such interactions include quartic self-interactions [19, 29, 47–55], axion-photon coupling [56–59], and electron-positron pair production [48, 84, 85]. Notably, if the coupling strengths are sufficiently weak, the BH may spin down before the cloud reaches saturation, allowing high-spin BHs to exclude these regions of parameter space.

One notable example involves the axion, characterized by a cosine potential $V \approx -\mu^2 f_\phi^2 \cos(\phi/f_\phi)$, where f_ϕ denotes the axion decay constant. The self-interactions stemming from this potential, particularly the quartic term $V \supset -\lambda\phi^4 \equiv -\phi^4\mu^2/(24f_\phi^2)$, quench the exponential growth into a saturated state. In this state, the superradiant ground mode field value stabilizes at $\Psi_0^\lambda \approx \alpha f_\phi/2$, resulting in steady axion waves radiating towards infinity [29, 47, 49]. This mechanism sets another threshold for the total cloud mass, distinct from the spin-down requirement of $10\%M_{\text{BH}}$.

This study investigates the direct couplings between a bosonic cloud and fermions. The intense field within the cloud can trigger the parametric production of fermions, which may then undergo further acceleration as they propagate through the cloud. This process potentially leads to a saturated cloud state that efficiently converts the rotational energy of the BH into fermion emissions.

2.2 Particle Production from Boson Condensates

In this section, we review parametric matter production from oscillating scalar backgrounds and Schwinger pair production from vector backgrounds. We also discuss how these mechanisms apply to superradiant clouds.

2.2.1 Parametric Matter Production from Scalar Backgrounds

We begin by considering a bosonic field χ in a time-varying background [60, 61, 86, 87]. The equation of motion for χ in the frequency domain is given by:

$$\ddot{\chi}_k + \omega_k(t)^2 \chi_k = 0. \quad (2.4)$$

Here, $\omega_k(t)$ represents the time-varying energy, modulated by the background fields to which χ couples. The solutions to this equation in the adiabatic representation are expressed as [87]:

$$\chi_k(t) = \frac{\alpha_k(t)}{\sqrt{2\omega_k}} e^{-i \int_0^t \omega_k dt} + \frac{\beta_k(t)}{\sqrt{2\omega_k}} e^{+i \int_0^t \omega_k dt}. \quad (2.5)$$

The coefficients α_k and β_k evolve according to:

$$\dot{\alpha}_k = \frac{\dot{\omega}_k}{2\omega_k} e^{+2i \int_0^t \omega_k dt} \beta_k, \quad \dot{\beta}_k = \frac{\dot{\omega}_k}{2\omega_k} e^{-2i \int_0^t \omega_k dt} \alpha_k, \quad (2.6)$$

and they adhere to the normalization condition $|\alpha_k|^2 - |\beta_k|^2 = 1$. At $t = 0$, the vacuum state is defined by $\alpha_k = 1$ and $\beta_k = 0$. The quantities $\alpha_k(t)$ and $\beta_k(t)$ correspond to the coefficients of the Bogoliubov transformation, which diagonalize the Hamiltonian at each moment t . The particle occupation number for a momentum mode k is given by $n_k = |\beta_k|^2$, and the particle number density per unit volume is:

$$n_\chi = \frac{1}{2\pi^2} \int_0^\infty dk k^2 |\beta_k|^2. \quad (2.7)$$

For $|\beta_k| \ll 1$, the solution for Eq. (2.6) can be approximated as:

$$\beta_k \simeq \int_0^t dt' \frac{\dot{\omega}}{2\omega} \exp\left(-2i \int_0^{t'} dt'' \omega(t'')\right). \quad (2.8)$$

Consequently, efficient particle production occurs when the non-adiabatic condition is satisfied:

$$\left| \frac{\dot{\omega}}{\omega^2} \right| \gg 1. \quad (2.9)$$

Using the interaction term $g_{S\chi}^2 \phi^2 \chi^2 / 2$ as an example, let us consider $\phi = \phi_0 \cos(\mu t)$ to represent the coherently oscillating background scalar field with amplitude ϕ_0 and frequency μ , and $g_{S\chi}$ to denote the coupling constant. The frequency relation for χ is [87]

$$\omega_\chi^2 = k^2 + m_\chi^2 + g_{S\chi}^2 \phi_0^2 \cos^2(\mu t). \quad (2.10)$$

Here, m_χ represents the bare mass term of χ . We concentrate on the regime where $g_{S\chi}^2 \phi_0^2 / \mu^2 \gg 1$, and the mass m_χ can be considered negligible. Within a narrow region of ϕ during a single oscillation period, momentum values below the typical scale $k_\star = \sqrt{g_{S\chi} \phi_0 \mu} / 2$ satisfy the non-adiabatic condition (2.9). Consequently, the occupation number n_k for $k < k_\star$ is exponentially produced with a time dependence of approximately $\exp(2\mu\tau_k t)$, where $\tau_k \approx \mathcal{O}(0.1)$ [87].

A fermionic field ψ with a Yukawa-like coupling $g_S \phi \bar{\psi} \psi$ and a bare mass m_ψ follows a frequency relation for their mode function described by [60, 61]:

$$\omega_\psi^2 = k^2 + (m_\psi + g_S \phi_0 \cos(\mu t))^2 - i g_S \mu \phi_0 \sin(\mu t). \quad (2.11)$$

In regions with a dense boson background, where the resonance parameter $q \equiv g_S^2 \phi_0^2 / \mu^2$ is significantly high and $g_S \phi_0 \gg m_\psi$, the non-adiabatic condition is met when the effective mass term, $m_{\text{eff}} \equiv m_\psi + g_S \phi_0 \cos(\mu t)$, crosses zero. During each crossing, the background substantially contributes to the k -mode with a factor of $|\beta_k|^2 = e^{-\pi k^2 / (g_S \phi_0 \mu)} + \dots$, where \dots accounts for contributions from previously produced fermions [60, 61]. Exponential growth is precluded due to Pauli blocking. Instead, a fermion sphere with a radius approximately $k_F = \sqrt{g_S \phi_0 \mu} / 2$ forms immediately after each interaction.

For fermions produced from a locally dense scalar condensate, those generated during the previous interaction are accelerated to much higher energy scales, a topic further discussed in the subsequent subsection, without hindering new production. Consequently, the average pair production rate per unit volume is estimated as:

$$\Gamma_{\phi\psi} \approx \frac{1}{2\pi^2} \frac{k_F^3}{3} \frac{\mu}{\pi} = \frac{g_S^2 \phi_0^2 \mu^2}{48\pi^3} \sqrt{\frac{\mu}{g_S \phi_0}}. \quad (2.12)$$

The factor π/μ represents the time interval between two zero crossings. Additionally, when the de Broglie wavelength of the initially produced fermions, approximately $2\pi/k_*$, is considerably shorter than the condensate size, the finite size of the boson background can be disregarded in calculating the production rate, akin to the production of millicharged particles from superconducting cavities [88].

This parametric excitation of fermion and anti-fermion pairs is more efficient than perturbative decay, especially since an ultralight scalar cannot decay into fermions heavier than itself through perturbative processes.

One fundamental distinction between boson and fermion production lies in the requirement for the bare mass term. In Eq. (2.11), the effective mass is the linear sum of the bare mass and the oscillating term, necessitating only that $g_S \phi_0 \gg m_\psi$ to facilitate parametric excitation [61]. Conversely, for bosons, the bare mass m_χ must be smaller than k_* due to their analogous roles in influencing the dynamics as detailed in Eq. (2.10). Consequently, heavier fermions can be parametrically excited compared to bosons.

2.2.2 Schwinger Pair Production from Vector Backgrounds

We next consider a charged scalar field σ in a static electric background along the z -axis, specifically $A_z = Et$ in the temporal gauge. The dispersion relation is given by

$$\omega_\sigma^2 = (k_z - eEt)^2 + k_\perp^2 + m_\sigma^2, \quad (2.13)$$

where e represents the charge of σ , k_\perp denotes its momentum transverse to the z -axis, and m_σ is its mass. When $eE \gg m_\sigma^2$, we can disregard the mass term and anticipate the production of relativistic σ particles. Considering the non-adiabatic condition (2.9) once again, we observe that modes with $0 < k_z \leq \sqrt{eE}$ and $k_\perp \ll \sqrt{eE}$ satisfy it at $t = 0$. These modes continue to satisfy the condition until approximately $t \approx 1/\sqrt{eE}$, at which point the corresponding occupation number becomes saturated due to the balance between production and acceleration towards higher energies. The presence of $k_\perp^2 + m_\sigma^2$ introduces an exponential suppression factor to the occupation number, providing an approximation to the production rate [89]:

$$\begin{aligned} \Gamma_{Schw} &\approx \sqrt{eE} \int \frac{d^3 \vec{k}}{(2\pi)^3} \exp\left(-\frac{\pi(m_\sigma^2 + k_\perp^2)}{eE}\right) \text{H}(\sqrt{eE} - k_z) \text{H}(k_z) \\ &= \frac{e^2 E^2}{8\pi^3} \exp\left(-\frac{\pi m_\sigma^2}{eE}\right), \end{aligned} \quad (2.14)$$

where H is the Heaviside function. The factor $1/\sqrt{eE}$ denotes the production timescale. A more complete sum introduces an additional factor of $\sum_{n=1}^{\infty} 1/n^2 = \pi^2/6$ when $eE \gg m_\sigma^2$ [62].

For a localized vector condensate characterized by a mass μ , the Schwinger pair production rate is independent of whether the produced particles are bosons or fermions, as the occupation number remains low for $k \leq k_\star = \sqrt{eE}$. Any produced pair is immediately accelerated to higher momenta. Additionally, the de Broglie wavelength, approximately $2\pi/k_\star$, and the production timescale are notably shorter than the condensate's size and its oscillation period, given that $k_\star \gg m_\psi \gg \mu$. In this context, the finite size and periodic oscillation of the condensate can be disregarded when considering the production rate, which simplifies the analysis of the condensate's particle dynamics.

2.2.3 Fermion Production from Boson Clouds

We now turn our attention to the superradiant scalar and vector clouds discussed in Sec. 2.1, focusing on their interactions with fermions ψ through Yukawa-like and Abelian gauge interactions, respectively. Within both types of clouds, fermion pairs can spontaneously emerge, driven by the light masses of the fermions and the substantial field values of the bosons.

The spatially dependent scalar field ϕ introduces a coherently oscillating mass term, $g_S\phi$, to the fermions, in addition to their bare mass, m_ψ . When the product $g_S\phi_0$ surpasses m_ψ , the effective mass, $m_{\text{eff}} \equiv g_S\phi + m_\psi$, oscillates through zero twice each period. At each zero-crossing, fermions undergo parametric excitation, populating a fermion sphere with a radius $k_F \approx \sqrt{g_S\phi_0\mu}/2$. This calculation assumes that the fermion's de Broglie wavelength, approximately $1/k_F$, is significantly shorter than the cloud's size, approximately $1/(\alpha\mu)$, allowing the neglect of finite-size effects. The scalar cloud also exhibits an oscillatory component in its wavefunction, dependent on the azimuthal angle, i.e., $\phi \propto \cos(\mu t - \varphi)$. This dependence stems from the orbital angular momentum of the cloud. Notably, at a specific time t , the non-adiabatic condition is triggered on a plane approximately aligned with $\varphi = \mu t \pm \pi/2$. Consequently, the cloud's oscillation induces a periodic rotation of the production plane around the spin axis of the BH.

Similarly, vector clouds with gauge interaction $g_V A'^\mu \bar{\psi} \gamma_\mu \psi$ may produce fermions through Schwinger pair production when the electric field strength, $E_{A'} \approx \mu |\vec{A}'|$, is high enough that $g_V E_{A'} \gg m_\psi^2$ [62], where g_V denotes the interaction strength. In this scenario, the produced fermions carry momentum approximately $\sqrt{g_V E_{A'}}$, with their directions either aligned or anti-aligned with the electric field direction. These particles are then accelerated by the electric field to energies about $\omega_{\text{acc}}^\psi \sim g_V E_{A'}/\mu$, as will be explored further in the next subsection. In this context, the phenomenon of Pauli blocking is negligible, primarily due to the significant difference between ω_{acc}^ψ and the initial momentum $\sim \sqrt{g_V E_{A'}}$.

In summary, the average pair production rates per unit volume for each fermion state in these processes are given by:

$$\Gamma_{S\psi} \approx \frac{g_S^2 \phi_0^2 \mu^2}{48\pi^3} \sqrt{\frac{\mu}{g_S \phi_0}}, \quad \Gamma_{V\psi} \approx \frac{g_V^2 E_{A'}^2}{48\pi}, \quad (2.15)$$

where ϕ_0 and $E_{A'}$ are influenced by the cloud wavefunctions, which exhibit spatial and temporal variations.

2.3 Fermion Acceleration and Resulting Fluxes from Boson Clouds

To analyze the emitted fermion spectrum and energy extraction from superradiant clouds, it is essential to consider their propagation immediately after production. Both non-uniform scalar clouds and the electric components of vector clouds can exert forces on the produced fermions, accelerating them to significantly higher energies. As discussed in Sec. 2.2, we consider the scenario where the fermion de Broglie wavelength, $< 1/\sqrt{g_{S/V}\Psi_0\mu}$, is considerably smaller than both the cloud size, $\sim r_g/\alpha^2 = 1/(\mu\alpha)$, and the oscillation timescale, $\sim 1/\mu$. This allows us to model each fermion as a point-like particle and use the worldline equation of motion to study their propagation.

Upon their production, fermions begin their propagation through the bosonic field surrounding the BH. This scenario is akin to analyzing geodesics with a variable mass term, $m_{\text{eff}} = g_S\phi + m_\psi$ for scalar clouds, or considering a charged particle influenced by both the electromagnetic field of the vector cloud and the BH's gravitational potential. The worldline action governing the fermion's trajectory is described by:

$$S_\psi = \begin{cases} - \int d\tau |m_{\text{eff}}| \sqrt{-g_{\alpha\beta} u_\psi^\alpha u_\psi^\beta}, & \text{Scalar} \\ - \int d\tau \left(m_\psi \sqrt{-g_{\alpha\beta} u_\psi^\alpha u_\psi^\beta} \mp g_V A'_\beta u_\psi^\beta \right), & \text{Vector} \end{cases}, \quad (2.16)$$

where $g_{\alpha\beta}$ is the Kerr metric and u_ψ^α is the fermion's four-velocity. The symbol \mp differentiates fermion from antifermion. From this action, the Euler-Lagrange equation is derived as:

$$\frac{du_\psi^\alpha}{d\tau} = -\Gamma_{\kappa\beta}^\alpha u_\psi^\kappa u_\psi^\beta + \begin{cases} - (g^{\alpha\beta} + u_\psi^\alpha u_\psi^\beta) \frac{\nabla_\beta m_{\text{eff}}}{m_{\text{eff}}}, & \text{Scalar} \\ \pm u_\psi^\beta \frac{g_V F'^\alpha_\beta}{m_\psi}, & \text{Vector} \end{cases}, \quad (2.17)$$

where τ signifies the proper time, the Christoffel symbols, $\Gamma_{\kappa\beta}^\alpha$, pertain to the Kerr metric, and F'^α_β represents the field tensor for A'^μ . By applying the relations $dt = u_\psi^0 d\tau$ and $p_\psi^\alpha = |m_{\text{eff}}| u_\psi^\alpha$ (scalar) or $m_\psi u_\psi^\alpha$ (vector), we can reformulate this equation as

$$\frac{dp_\psi^\alpha}{dt} = -\frac{1}{p_\psi^0} \Gamma_{\kappa\beta}^\alpha p_\psi^\kappa p_\psi^\beta + \begin{cases} - \nabla^\alpha m_{\text{eff}}^2 / (2p_\psi^0), & \text{Scalar} \\ \pm g_V (\vec{E}_{A'} + \vec{v}_\psi \times \vec{B}_{A'}), & \text{Vector} \end{cases}, \quad (2.18)$$

where p_ψ^α represents the fermion's four-momentum and \vec{v}_ψ its velocity. The electric and magnetic fields, $\vec{E}_{A'}$ and $\vec{B}_{A'}$, are defined by $\vec{E}_{A'} \equiv -\nabla A'^0 - \partial_t \vec{A}'$ and $\vec{B}_{A'} \equiv \nabla \times \vec{A}'$, respectively.

In both scenarios, fermions can be accelerated to energies on the order of $g_{S/V}\Psi_0$, significantly surpassing their initial momentum, approximately $\sqrt{g_{S/V}\Psi_0\mu}$. Consequently, the Pauli blocking effect can be disregarded for both the production rate and the acceleration process. Furthermore, considering that the production timescale and the initial de Broglie wavelength of the fermion, approximately $1/\sqrt{g_{S/V}\Psi_0\mu}$, are considerably shorter than the cloud's oscillation period, roughly $2\pi/\mu$, and the cloud's size, approximately $1/(\alpha\mu)$, the effects of the cloud's finite size and temporal variance can be safely overlooked. This is similar to the production mechanisms of millicharged particles from superconducting cavities [88].

Additionally, we should ensure that the backreaction of fermions on the bosonic cloud can be neglected. Around a vector field, the recoil power on a relativistic fermion in the strong

field limit $g_V E_{A'} \gg m_\psi^2$ is typically on the order of $g_V^{8/3} E_{A'}^{2/3} \omega_{\text{acc}}^{\psi 2/3} \sim g_V^{10/3} \Psi_0^{4/3} \mu^{2/3}$ [90–92]. Compared to the boson cloud’s acceleration power $\sim g_V \Psi_0 \mu$, it requires $g_V \ll (\mu/\Psi_0)^{1/7}$. For astrophysical BHs, superradiant μ is between 10^{-21} to 10^{-11} eV and the field value $\Psi_0 < 10^{17}$ GeV and a value of $g_V \ll 10^{-8}$ can easily satisfy this condition.

The forces influencing fermion trajectories in Eq. (2.18) include gravitational deflection and either the scalar force [93] or electromagnetic forces from a vector cloud. For scalar clouds, we analyze their comparative impacts in Cartesian coordinates (t, x, y, z) :

$$-\frac{\Gamma_{\kappa\beta}^\alpha p_\psi^\kappa p_\psi^\beta}{m_{\text{eff}}^2/r_g} \approx -\frac{r_g^2}{r^2} \left(\mathcal{O}(1) + \mathcal{O}\left(\frac{r_g}{r}\right) \right), \quad (2.19)$$

$$-\frac{\vec{\nabla} m_{\text{eff}}^2}{m_{\text{eff}}^2/r_g} = \alpha^2 \hat{r} - \frac{2r_g}{r \cos(\alpha t - \phi) \sin \theta} \hat{n}_\perp + \dots \quad (2.20)$$

Here, \dots denotes the minor impact of the fermion’s bare mass term m_ψ in regions where $g_S \phi_0 \gg m_\psi$. The vector $\hat{n}_\perp \equiv (\cos(\alpha t), \sin(\alpha t), 0)$ represents a unit directional vector rotating in the $x - y$ plane. It becomes evident that in most parts of the cloud, the scalar force exceeds gravitational lensing in influence. For vector clouds, a similar quantitative assessment applies in the cloud’s dominant region ($r^2 > r_g^2/\alpha$). Consequently, we will neglect the gravitational deflection’s effect in our simulation.

We proceed by simulating neutrino trajectories and capturing the flux at infinity, introducing dimensionless quantities for convenience:

$$(\tilde{t}, \tilde{x}, \tilde{y}, \tilde{z}) \equiv \left(\frac{t}{r_g}, \frac{x}{r_g}, \frac{y}{r_g}, \frac{z}{r_g} \right), \quad \tilde{p}_\psi^\alpha \equiv \frac{p_\psi^\alpha}{g_{S/V} \Psi_0}, \quad \tilde{m}_\psi \equiv \frac{m_\psi}{g_{S/V} \Psi_0}, \quad \tilde{m}_{\text{eff}} \equiv \frac{m_{\text{eff}}}{g_S \Psi_0}, \quad \vec{\tilde{E}}_{A'} \equiv \frac{\vec{E}_{A'}}{\Psi_0}, \quad \vec{\tilde{B}}_{A'} \equiv \frac{\vec{B}_{A'}}{\Psi_0}. \quad (2.21)$$

This redefinition allows us to describe the trajectories as follows:

$$\frac{d\vec{\tilde{x}}}{d\tilde{t}} = \frac{\vec{\tilde{p}}_\psi}{\tilde{p}_\psi^0} = \vec{v}_\psi, \quad \begin{cases} \frac{d\vec{\tilde{p}}_\psi}{d\tilde{t}} = -\frac{\vec{\nabla} \tilde{m}_{\text{eff}}^2}{2\tilde{p}_\psi^0}, & \text{Scalar} \\ \frac{d\vec{\tilde{p}}_\psi}{d\tilde{t}} = \pm g_V (\vec{\tilde{E}}_{A'} + \vec{v}_\psi \times \vec{\tilde{B}}_{A'}), & \text{Vector} \end{cases} \quad (2.22)$$

Utilizing a Monte Carlo simulation, we generate fermion events, distributing initial positions within the range $2 < r/r_g < 40/\alpha^2$, the latter significantly exceeding the cloud’s Bohr radius. The generalized acceptance-rejection method [94] is applied to a distribution weighted by the production rate $\Gamma_{S\psi} \propto \phi_0^{3/2}$ for scalar fields and $\Gamma_{V\psi} \propto E_{A'}^2$ for vector fields. Setting the initial time of each event to $\tilde{t} = 0$ for simplicity, fermion production from a scalar cloud is concentrated in planes at $\varphi = \pm\pi/2$, whereas vector cloud production spans the entire wavefunction.

To evolve the trajectory of each event using Eq. (2.22), we need to specify the initial dimensionless momentum on the order of $\sim \sqrt{\mu/(g_{S/V} \Psi_0)}$ and the fermion’s bare mass, \tilde{m}_ψ . In a scalar cloud, fermions are generated when \tilde{m}_{eff} is close to zero, with their initial momentum isotropically distributed. Conversely, in a vector cloud, the initial fermion momentum either aligns or anti-aligns with the electric fields. Both the initial momentum and \tilde{m}_ψ are significantly less than 1 in the parameter space relevant to this study. Testing for trajectory convergence demonstrated that outcomes are independent of the initial momentum values, as the bosonic cloud quickly adjusts $|\vec{\tilde{p}}_\psi|$ to $\mathcal{O}(1)$ values. Consequently, we choose a sufficiently small initial momentum and set both \tilde{m}_{eff} and \tilde{m}_ψ to zero for the initial conditions.

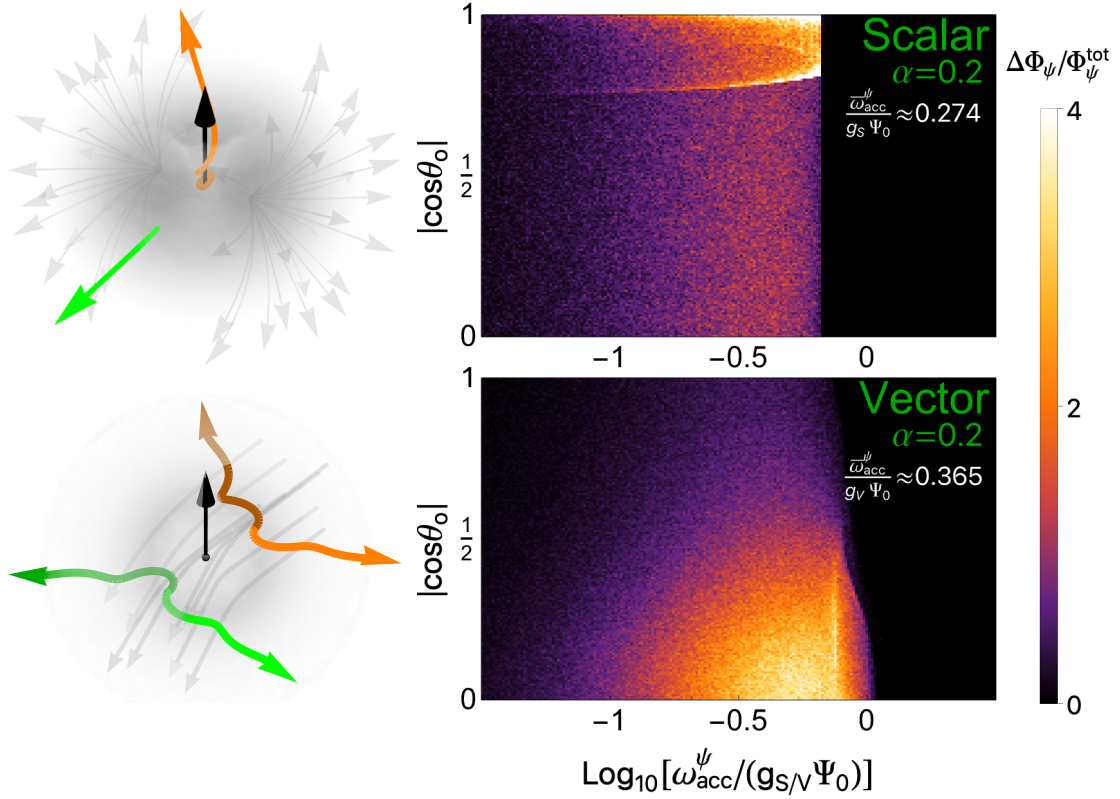


Figure 1: Top left: Examples of fermion trajectories originating simultaneously from distances of $10r_g$ (orange) and $100r_g$ (green) relative to a BH surrounded by a scalar cloud, with α set at 0.2. The black arrow indicates the direction of the BH’s spin, and the cloud’s energy density alongside the initial scalar force lines are depicted in gray. Top right: The observed fermion energy spectrum $\Delta\Phi_\psi \equiv d\Phi_\psi/(d\cos\theta_o d\log_{10}\omega_{\text{acc}}^\psi)$ across various inclination angles θ_o , with Φ_ψ^{tot} representing the total emitted flux. The average energy of emitted fermions, $\bar{\omega}_{\text{acc}}^\psi$, is on the order of $g_S\Psi_0$. Bottom: Analogous to the top panels but for a vector cloud. Here, trajectories in green and orange represent fermion paths from $30r_g$, with green tracing the equatorial plane and orange at $\theta = \pi/4$. Light and dark hues distinguish between fermions and anti-fermions, respectively.

The trajectory analysis concludes at $\tilde{t} = 400/\alpha^2$, where both the momentum and the outgoing direction (θ, φ) converge to nearly constant values. Assuming the observation duration exceeds the oscillation period $2\pi/\mu$, the impact of the azimuthal angle φ on the event can be disregarded. For a vector cloud, fermion and anti-fermion fluxes are identical, as the trajectory of an anti-fermion mirrors that of a fermion originating from the same point but beginning a half-period π/μ later, aligning with a phase shift in the boson wavefunction. The final momentum and polar angle are documented as $\omega_{\text{acc}}^\psi/(g_{S/V}\Psi_0) \equiv \tilde{p}_\psi^0$ and $\cos\theta_o \equiv \tilde{p}_\psi^z/\tilde{p}_\psi^0$, respectively.

An example depicted in the top left panel of Fig. 1 illustrates trajectories emanating from $10r_g$ (orange) and $100r_g$ (green) within a scalar cloud of $\alpha = 0.2$. Additionally, we depict the force lines at the production time and scalar density in gray. Notably, the trajectory originating from the outer region exits the cloud directly in the radial direction, while the trajectory closer to the BH first curls around the BH spin axis (black arrow). This occurs

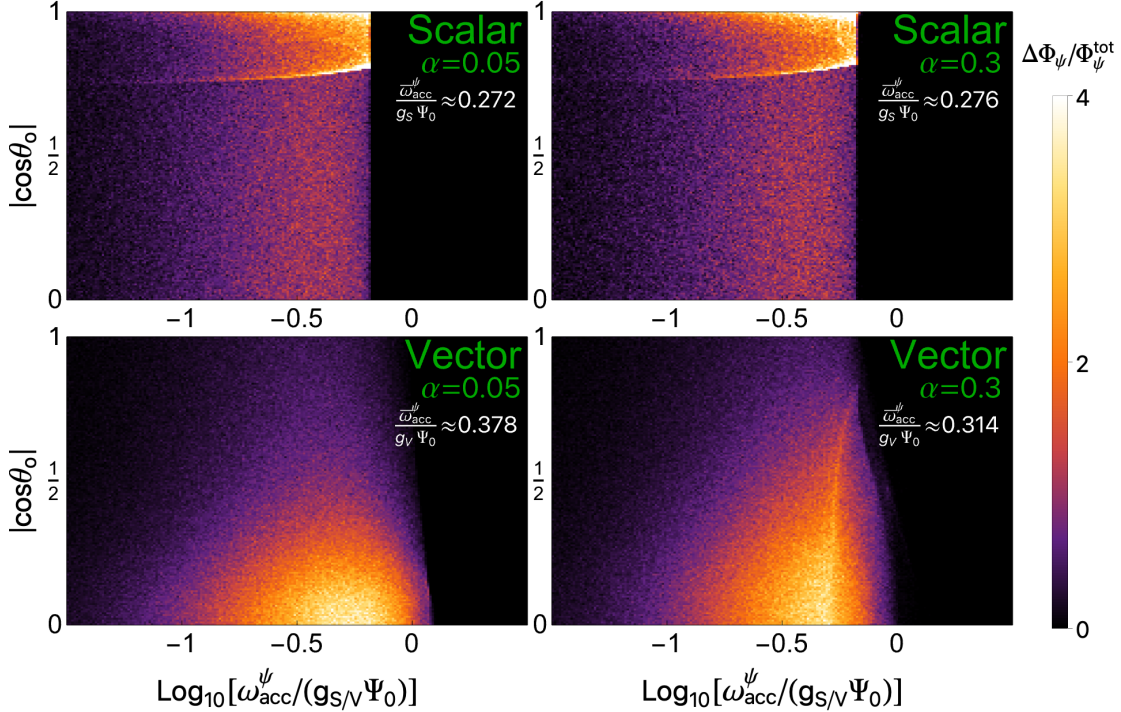


Figure 2: Same as Fig. 1 with $\alpha = 0.05$ and 0.3 .

because fermions produced at larger radii predominantly experience acceleration in the radial direction due to the first term on the right-hand side of Eq. (2.20), resulting in an almost isotropic flux distribution for $|\cos \theta_o| < 3/4$. Conversely, in the cloud's inner region, the second term of Eq. (2.20) becomes significant, confining trajectories to areas with small inclination angles ($|\cos \theta_o| > 3/4$) and leading to a noticeable increase in fermion flux. The top right panel illustrates the outgoing spectrum as a function of the observer's inclination angle, θ_o , highlighting a jet-like structure of fermions with higher flux observed from nearly face-on angles ($|\cos \theta_o| > 3/4$), attributed to fermions produced closer to the cloud's center being funneled along the polar axis. Our simulations indicate an average energy for the fermion fluxes of $\bar{\omega}_{\text{acc}}^{\psi}/(g_S \Psi_0) \approx 0.274$. In Fig. 2, we compare results for $\alpha = 0.05$ and 0.3 . Notably, both the spectrum and average momentum demonstrate minimal dependence on α .

For the vector cloud, we illustrate examples of both fermion (light) and anti-fermion (dark) trajectories in the bottom left panel of Fig. 1, with the outgoing spectrum showcased in the bottom right panel. The distribution of the spectrum across inclination angles θ_o reveals distinct behaviors between scalar and vector clouds. In vector clouds, acceleration is primarily influenced by electric fields, which are predominantly perpendicular, resulting in a greater flux directed towards observers in an edge-on position, where $\cos \theta_o \approx 0$. Although magnetic fields may deflect trajectories towards higher latitude regions, their influence is reduced by a factor of α compared to that of electric fields. Nevertheless, fluxes towards face-on observers ($|\cos \theta_o| \approx 1$) remain substantial due to these deflections. The α -dependence is again minor, as demonstrated in Fig. 2.

Through this analysis, the resultant average energy of the fermion fluxes, $\bar{\omega}_{\text{acc}}^{\psi}$, is given

by

$$\bar{\omega}_{\text{acc}}^{\psi} \approx \begin{cases} 0.27 g_S \Psi_0, & \text{Scalar} \\ 0.35 g_V \Psi_0, & \text{Vector} \end{cases}, \quad (2.23)$$

which is generally independent of the parameter α .

The differential fermion fluxes observable by a distant observer can be estimated as follows:

$$\begin{aligned} \frac{d\Phi_{\psi}}{d\omega_{\text{acc}}^{\psi}(\bar{\omega}_{\text{acc}}^{\psi})} &\approx \frac{2 N_{\psi} \int \Gamma_{S\psi/V\psi} d^3\vec{x}}{4\pi d^2 \bar{\omega}_{\text{acc}}^{\psi}} \\ &\approx \begin{cases} 1.2 \times 10^{-8} \text{ cm}^{-2}\text{s}^{-1}\text{GeV}^{-1} \left(\frac{\Psi_0/\text{GeV}}{4.8 \times 10^7}\right)^{1/2} \left(\frac{N_{\psi}}{3}\right) \left(\frac{10^{-12}}{\mu/\text{eV}}\right)^{1/2} \left(\frac{0.3}{\alpha}\right)^3 \left(\frac{g_S}{10^{-8}}\right)^{1/2} \left(\frac{5}{d/\text{kpc}}\right)^2, \\ 1.3 \times 10^3 \text{ cm}^{-2}\text{s}^{-1}\text{GeV}^{-1} \left(\frac{\Psi_0/\text{GeV}}{5.7 \times 10^{14}}\right) \left(\frac{N_{\psi}}{1}\right) \left(\frac{10^{-12}}{\mu/\text{eV}}\right) \left(\frac{0.3}{\alpha}\right)^3 \left(\frac{g_V}{10^{-12}}\right) \left(\frac{5}{d/\text{kpc}}\right)^2, \end{cases} \end{aligned} \quad (2.24)$$

for scalar and vector clouds, respectively, where the boson mass and α values correspond to a BH of $40 M_{\odot}$. Here, the factor of 2 accounts for the production of fermion pairs, N_{ψ} represents the number of fermion mass/ flavor eigenstates being produced and accelerated, and d is the distance between the BH and the observer. The numerical values are evaluated using the expression in the first line, with benchmark parameters for both scalar and vector cases. The resulting spectrum is centered around $\bar{\omega}_{\text{acc}}^{\psi}$, with a width of the same order, as shown in Figs. 1, 2. Additionally, while Eq. (2.24) assumes isotropic emission, the observed flux can vary with the observer's inclination angle, potentially fluctuating by an order of magnitude, as indicated in Figs. 1, 2. The large discrepancy between the scalar and vector cases arises primarily from the field values in these benchmark parameters, which are chosen to satisfy the potential saturation conditions discussed in the following sections.

Here, we adopt $N_{\psi} = 3$ for scalar fields and $N_{\psi} = 1$ for vector fields as our benchmark values to align with the neutrino analysis in subsequent sections. A deviation from these values does not significantly affect the qualitative results. Given the large galactic scale distance, approximately $d \sim \text{kpc}$, an approximately uniform distribution among the various flavor eigenstates can occur due to mixing.

2.4 Saturating Cloud States

The growth of a boson cloud may continue until the rate of energy loss from fermion emissions aligns with the rate of energy gain through BH superradiance. As discussed in Sec. 2, the energy loss rate, scaled as $\bar{\omega}_{\text{acc}}^{\psi} \Gamma_{S\psi/V\psi}$, results in $\Psi_0^{5/2}$ for scalar fields and Ψ_0^3 for vector fields. In contrast, the superradiant energy gain rate, given by $\Gamma_{\text{SR}} M_{\text{cloud}} \propto \Psi_0^2$, follows a lower power relation. Balancing these two processes determines a critical field value, Ψ_0^c , which can be dynamically reached from an initially exponential growth phase. During the saturation phase, the boson cloud functions to convert BH rotational energy into a steady stream of fermion emissions.

This balance relation is expressed as:

$$\Gamma_{\text{SR}} M_{\text{cloud}} = 2 N_{\psi} \bar{\omega}_{\text{acc}}^{\psi} \int \Gamma_{S\psi/V\psi} d^3\vec{x}. \quad (2.25)$$

Here, the left side represents the superradiant energy gain rate, while the right side quantifies the energy loss rate due to fermion emission. Solving this equation yields the critical field

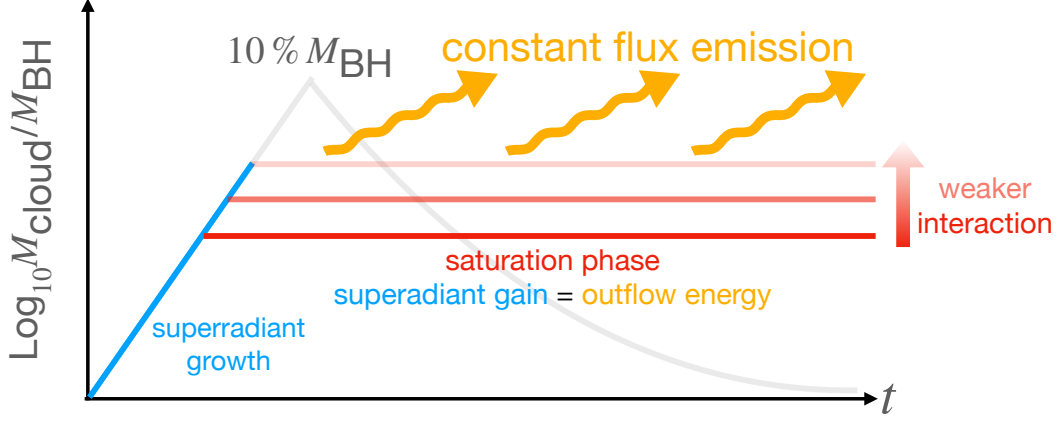


Figure 3: Illustration of an initially exponentially growing superradiant cloud transitioning into a saturation phase, depicted using the total cloud mass, M_{cloud} , as a function of time. The blue portion represents the superradiant growth phase, while the red lines indicate saturation phases where flux emission balances the superradiant energy gain from the BH. A lower coupling constant, $g_{S/V}$, leads to a higher critical field value, Ψ_0^c , as detailed in Eq. (2.26).

Ψ_0^c :

$$\Psi_0^c \approx \begin{cases} 4.8 \times 10^7 \text{ GeV} \left(\frac{3}{N_\psi} \right)^2 \left(\frac{\mu/\text{eV}}{10^{-12}} \right) \left(\frac{\alpha}{0.3} \right)^{16} \left(\frac{10^{-7}}{g_S} \right)^5 \left(\frac{a_J}{0.9} \right)^2, & \text{Scalar} \\ 5.7 \times 10^{14} \text{ GeV} \left(\frac{1}{N_\psi} \right) \left(\frac{\mu/\text{eV}}{10^{-12}} \right) \left(\frac{\alpha}{0.3} \right)^6 \left(\frac{10^{-12}}{g_V} \right)^3 \left(\frac{a_J}{0.9} \right), & \text{Vector} \end{cases}. \quad (2.26)$$

The benchmark parameters used here are in accordance with those from Eq. (2.24). Incorporating these parameters and the saturation field value from Eq. (2.26) into Eq. (2.23) and Eq. (2.24), we predict a steady fermion emission characterized by a typical energy scale in the TeV range for the vector case. The resultant fluxes are estimated to be around $10^3 \text{ cm}^{-2} \text{ s}^{-1} \text{ GeV}^{-1}$, markedly surpassing the TeV-scale atmospheric neutrino flux [82]. The discrepancy between the scalar and vector cases stems from the chosen benchmark parameters. However, even if the parameters are adjusted to equalize Ψ_0^c , the vector field can still dominate the energy emission rate due to the superradiant rate ratio $\sim 96/\alpha^2$ in the saturated limit.

An illustrative plot of this process is shown in Fig. 3, depicting the evolution of the total cloud mass over time. Initially, the cloud grows exponentially due to superradiance, then transitions to a saturation phase where steady fermion emissions balance the energy influx from BH superradiance. Notably, during the saturation phase, both the fermion fluxes and the average energy, $\bar{\omega}_{\text{acc}}^\psi$, increase due to a lower coupling constant, which results in a higher critical field Ψ_0^c , as detailed in Eq. (2.26).

The duration of the saturation phase can be estimated as $\sim M_{\text{BH}}/(\Gamma_{\text{SR}} M_{\text{cloud}})$, where $\Gamma_{\text{SR}} M_{\text{cloud}}$ represents the linear energy extraction rate. For the scalar case, using the benchmark values in Eq. (2.26), the estimated timescale is several orders of magnitude longer than the age of the universe. For the vector case, the saturation phase lasts a few days due to the

high benchmark field value. A shift in the benchmark parameter from $g_V = 10^{-12}$ to 10^{-11} significantly extends the saturation time to approximately a thousand years.

Whether a saturation state dominated by fermion emissions can be achieved depends on several factors. A straightforward requirement is that the critical field value Ψ_0^c should stay below $\Psi_0^{10\%}$, above which the saturation cannot be realized as the BHs' rotation already slows down. Another requirement comes from kinematics for parametric production— $g_S\Psi_0 \gg m_\psi$ for scalar fields and a more rigorous condition $\sqrt{g_V\Psi_0\mu} \gg m_\psi$ for vector fields.

Interactions with fermions lead to irreducible boson self-interactions that can quench exponential growth. For example, a Yukawa-type coupling generates a $\lambda\phi^4$ term through the Coleman-Weinberg mechanism, where $\lambda = g_S^4/(4\pi^2)$ [95]. When compared to a saturated axion state where $f_\phi = \mu/\sqrt{24\lambda}$, the critical field value Ψ_0^c should remain below $\Psi_0^\lambda \approx \alpha f_\phi/2 = \alpha\mu\pi/(2\sqrt{6}g_S^2)$. This requirement immediately rules out saturation under the benchmark parameters used in Eq. (2.26). Conversely, a vector field with a U(1) gauge interaction can induce only Euler-Heisenberg interactions, represented by $[(\vec{E}_{A'}^2 - \vec{B}_{A'}^2)^2 + 7(\vec{E}_{A'} \cdot \vec{B}_{A'})^2]g_V^4/(360\pi^2m_\psi^4)$ [96]. Due to the higher dimension operator, this results in a suppression factor of μ^4/m_ψ^4 compared to the scalar case, making this type of self-interaction inadequate for quenching superradiance within the parameters considered in this study.

Finally, the Yukawa interaction between the scalar cloud and fermions can significantly increase the fermions' effective mass, enabling decay processes that are kinetically forbidden in vacuum due to the low bare mass of the fermions. For instance, a standard model neutrino can decay into a charged pion and an electron or positron once its effective mass exceeds the mass of charged pions ($m_\pi \approx 140$ MeV), with the decay rate quickly surpassing the boson oscillation frequency $\sim \mu$. Consequently, the neutrino remains non-relativistic during its decay, drawing energy from the BH approximately equal to m_π rather than $g_S\Psi_0^c$. This scenario results in an energy loss rate proportional to $\Psi_0^{3/2}$, which is insufficient to balance the superradiant gain rate. Therefore, another condition emerges: $m_{\text{eff}} \sim g_S\Psi_0^c \ll m_{\text{dec}}$, where m_{dec} is the decay threshold. This issue does not occur with vector fields.

3 Spin Measurements for Neutrino-Boson Interaction

We now turn our attention to constraints on boson-fermion interactions. Within the Standard Model of particle physics, the coupling of most fermions to hidden ultralight bosons has been stringently constrained by experiments testing the fifth force, the equivalence principle, atomic clocks, and astrometry [97–107]. These constraints typically place $g_{S/V}$ well below 10^{-20} , making the critical field value Ψ_0^c from Eq. (2.26) significantly exceed $\Psi_0^{10\%}$, thereby preventing the saturation state from being reached. However, the mechanism of fermion production and acceleration by a bosonic cloud also extends to hidden sectors, where the coupling strength is often unconstrained.

A particularly notable case is that of the Standard Model neutrino, whose interactions with ultralight bosons are exceptionally challenging to detect due to difficulties in production, manipulation, and detection. We consider both scalar and vector interactions with neutrinos. The scalar field, often postulated as the Majoron, is motivated by mechanisms of neutrino mass generation [77, 108, 109], while the vector field stems from grand unification theories [78–80, 110, 111]. The interactions between these fields and the Standard Model neutrino, ν_L , in two-component spinor notation, are described as follows: [81]

$$\text{Scalar : } g_{S\nu} \phi \nu_L \nu_L; \quad \text{Vector : } g_{V\nu} A'^{\mu} \nu_L^\dagger \bar{\sigma}^\mu \nu_L. \quad (3.1)$$

We assume a universal coupling strength, $g_{S\nu}$ or $g_{V\nu}$, across all mass or flavor eigenstates. Note that the Majoron ϕ is typically assigned a lepton number of $L = -2$, while each ν_L carries $L = +1$.

Model-independent constraints on these couplings, particularly for ultralight bosons, primarily arise from neutrino self-interactions mediated by these bosons [81]. These constraints are largely unaffected by the boson’s mass μ when it is below the eV scale, and have been established through various observations including supernova (SN) 1987A [112–114], double beta decay [115, 116], big bang nucleosynthesis [117], and the cosmic microwave background (CMB) [118, 119]. Specifically, upper limits of $g_{S\nu} < 3 \times 10^{-7}$ have been inferred from SN 1987A [113, 114], and $g_{V\nu} < 7 \times 10^{-7}$ from the CMB [118]. Above the eV threshold, the variability of constraints in relation to the boson’s mass μ significantly increases [120–124].

There are scenarios where these couplings are subject to more stringent constraints: If bosons constitute a significant portion of dark matter, they could potentially alter neutrino oscillation patterns [95, 125–144]. Interactions between bosons and other Standard Model fermions also impose additional constraints [97, 100, 102–106]. Furthermore, when the fermion current is not conserved under the vector boson’s gauge group, physical processes are predominantly influenced by the vector’s longitudinal mode, leading to divergent constraints for an ultralight boson mass μ [145–151]. However, superradiant bosons need not make up the majority of dark matter, and through sophisticated model building, it is feasible to circumvent couplings to other Standard Model fermions and mitigate issues caused by the longitudinal mode. Therefore, our analysis will focus on model-independent constraints stemming from neutrino self-interactions.

Neutrino pairs can spontaneously emerge within both scalar and vector bosonic clouds, facilitated by light neutrino masses—the sum of the three mass eigenstates is less than 0.12 eV [152] and the lightest is unbounded from below [153]—coupled with the substantial field values of the bosons. The kinematic threshold for parametric production from scalar clouds, $g_{S\nu}\Psi_0 \gg m_\nu$, can be easily satisfied for all three neutrino mass eigenstates. For vector fields, the more stringent condition $\sqrt{g_{V\nu}\Psi_0\mu} \gg m_\psi$ is achievable for the lightest neutrino mass eigenstate in superradiant clouds around stellar-mass BHs. Consequently, we adopt $N_\nu = 3$ for scalar fields and $N_\nu = 1$ for vector fields as our benchmark values for N_ψ in Eqs. (2.24, 2.26), which have minor impacts on the quantitative results. At a galactic scale distance, $d \sim \text{kpc}$, the flux distribution among the three neutrino flavors tends to be approximately uniform due to neutrino oscillation effects.

To ensure uninterrupted superradiant energy transfer, the critical field value Ψ_0^c must remain below $\Psi_0^{10\%}$ to mitigate strong backreaction effects on BH rotation. This requirement defines an exclusion zone in parameter space for fast-rotating BHs that do not meet this criterion, particularly when the superradiant timescale is notably short compared to the BH’s evolutionary time. The focus is on rapidly rotating BHs, with confirmed masses ranging from $3 M_\odot$ to approximately $100 M_\odot$, evidenced by recent observations including X-ray binaries with significant separations [154], microlensing [155, 156], gravitational wave observations [157], and spectroscopic data such as iron lines that further inform on BH spins [158]. Moreover, the Event Horizon Telescope, with its unprecedented angular resolution, has captured horizon-scale images of two nearby supermassive BHs: M87* ($6.5 \times 10^9 M_\odot$) [159] and Sgr A* ($4.3 \times 10^6 M_\odot$) [160], supporting high spins for these BHs. In our analysis, we consider dimensionless spins a_J ranging from 0.8 to 0.9, with corresponding maximum α values of 0.25 and 0.31 for these spins, respectively.

We consider the exclusion criterion where $\Psi_0^c > \Psi_0^{10\%}$, which allows high-spin BHs to

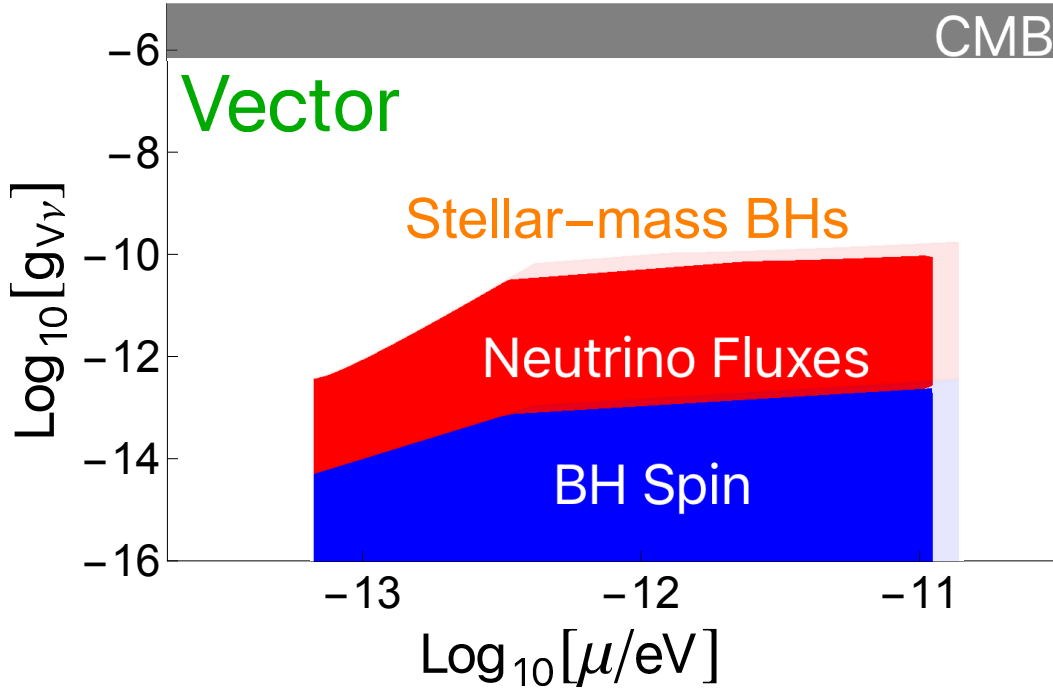


Figure 4: Prospects for constraining neutrino-vector couplings, $g_{\nu\nu}$. We consider a stellar-mass BH population with masses ranging from $3 M_{\odot}$ to $100 M_{\odot}$. The blue region marks the exclusion zone derived from BH spin measurements, with darker shades for a spin parameter $a_J = 0.8$ and lighter shades extending to $a_J = 0.9$, highlighting the impact of spin measurement uncertainties. The red region denotes areas where observable neutrino fluxes are expected from a target BH situated at a distance of 5 kpc. For reference, previous exclusions based on observations from the CMB [118] are shown in gray.

rule out the corresponding superradiant parameter space. In Fig. 4, we illustrate the spin measurement constraints for the vector-neutrino coupling $g_{\nu\nu}$ using the population of stellar-mass BHs. The dark blue region denotes constraints for a dimensionless spin parameter $a_J = 0.8$, while the light blue represents the expanded exclusion zone for $a_J = 0.9$. The analysis begins with a lower limit for α at 0.05. The boson mass, defined as $\mu \equiv \alpha/(G_N M_{\text{BH}})$, is divided into two regions. In the low-mass segment, we set $M_{\text{BH}} = 100 M_{\odot}$ and vary α from 0.05 up to its upper limits of 0.25/0.31. In the high-mass section, α is fixed at 0.25/0.31, and M_{BH} is adjusted from $100 M_{\odot}$ down to $3 M_{\odot}$. For SMBHs, boson masses below 10^{-17} eV face challenges in meeting the kinetic conditions for relativistic Schwinger pair production, making them difficult to consider in this context. This quantitative exclusion also applies to dark fermions whose mass meets the kinematic threshold.

The dynamics of the scalar-neutrino interaction, as discussed in Sec. 2.4, involve complex phenomena including quartic self-interactions induced by neutrino loops. This interaction introduces a threshold $\Psi_0^\lambda = \alpha\mu\pi/(2\sqrt{6}g_{S\nu}^2)$, which is significantly lower than Ψ_0^g when $g_{S\nu} \ll 10^{-7}$. As a result, a saturation state driven by scalar quartic self-interactions is expected, with predominant fluxes from scalar emissions rather than neutrino emissions. Therefore, spin measurements can only exclude regions where $\Psi_0^\lambda > \Psi_0^{10\%}$, which translates to weak constraints on $g_{S\nu}$, typically $g_{S\nu} \ll 10^{-18}$ for boson masses around 10^{-12} eV, and even weaker for scalar masses associated with SMBHs.

4 Neutrino and Boosted Dark Matter Fluxes from Superradiant Clouds

For couplings beyond the limits set by spin measurements, a saturated vector cloud consistently emitting neutrino fluxes is expected. Once the critical field value, Ψ_0^c , is determined from Eq. (2.26), the neutrino flux spectrum for a specific BH can be calculated using Eq. (2.24), factoring in the BH’s distance from Earth d , and the observer’s inclination angle θ_o . Considering a benchmark scenario with parameters $\mu = 10^{-12}$ eV, $M_{\text{BH}} = 40 M_\odot$, $d = 5$ kpc, $g_{V\nu} = 10^{-12}$, and $a_J = 0.9$, we find $\Psi_0^c \approx 5.7 \times 10^{14}$ GeV. This leads to TeV-scale neutrino fluxes around $10^3 \text{ cm}^{-2}\text{s}^{-1}\text{GeV}^{-1}$, substantially exceeding the atmospheric neutrino flux at TeV energies [82]. The neutrino fluxes and their average energy increase during the saturation phase as $g_{V\nu}$ decreases, attributable to a lower $g_{V\nu}$ yielding a higher critical amplitude Ψ_0^c .

With the cessation of exponential BH spin energy extraction by the cloud, a high-spin BH can coexist with a saturated cloud. Consequently, we maintain a_J values ranging from 0.8 to 0.9, while μ is categorized as per the spin measurement analysis. Given the wide distribution of BH candidates throughout the Milky Way, we set a standard distance of $d = 5$ kpc for analyzing the fluxes from a target BH. In Fig. 4, the red region denotes where neutrino fluxes from a saturated cloud are observable. The upper boundary is determined by requiring that neutrino fluxes at $\bar{\omega}'_{\text{acc}}$ exceed 1% of the diffusive neutrino background [82], aligned with the current IceCube angular resolution of $< 10^\circ$ [161, 162].

Neutrino production from a bosonic cloud is also applicable to other coupled fermions in the hidden sector. Moreover, dark matter particles within the vicinity of the cloud can be directly accelerated to higher energies. Thus, the superradiant cloud can act as a source for boosted dark matter, presenting opportunities for detection through direct detection experiments and neutrino detectors [63–76]. The specific incoming directions of these particles could lead to daily modulation of signals due to their interaction with Earth materials [163–168] or when captured by directional detectors [169].

In the case of scalar clouds, while scalar emissions are dominant, steady subleading fermion fluxes can also be expected. Detecting both spectra could help elucidate the origin of scalar self-interactions.

5 Discussion

Strong fields serve as a fertile ground for exploring various fascinating phenomena, notably particle production. These phenomena have been studied within the early universe’s preheating phase [60, 61] and the domain of strong field quantum electrodynamics [62]. Rotating BHs offer an exceptional platform for such explorations, especially as superradiant clouds around them can attain field values nearing the Planck scale.

This study examines the interactions between ultralight bosonic fields and fermions facilitated by BH superradiance. Dense superradiant bosonic clouds are shown to efficiently generate and accelerate fermions, encompassing both scalar and vector types. We specifically delve into neutrino-boson interactions, approached from two angles: BH spin measurements can exclude interactions with very weak couplings, while observations of neutrino fluxes from high-spin BHs can help define the boundaries of strong interactions.

We demonstrate that neutrino fluxes emitted from a nearby stellar-mass BH, surrounded by a vector cloud, can significantly surpass the diffusive background [82, 170–173]. Additionally, interactions between bosons and hidden-sector fermions could result in the emission of

boosted dark matter fluxes. This opens a new frontier in multi-messenger astronomy: electromagnetic and gravitational wave observations identify BHs and ascertain their masses, spins, and inclination angles, while neutrino [161, 162, 174–182] and dark matter detectors [63–76, 163–168] focus on these BHs to monitor the resulting flux emissions.

The current generation of neutrino detectors, such as IceCube [161, 162], ANTARES [174], and Baikal-GVD [175], has already shown significant sensitivity in searching for point-like sources. Future detectors, including KM3NeT [176], P-ONE [177], IceCube-Gen2 [178], and TRIDENT [179], are expected to further enhance angular resolution and offer more comprehensive sky coverage. Their performance is notably improved when integrated into a global network, boosting our capability to detect and analyze these intriguing phenomena [183].

Acknowledgements

We are grateful to Markus Ahlers, Zhaoyu Bai, Mauricio Bustamante, Shao-Feng Ge, Minyuan Jiang, Qinrui Liu, Yuxin Liu, Luca Visinelli, Xin Wang, Donglian Xu and Xunjie Xu for useful discussions. This work is supported by VILLUM FONDEN (grant no. 37766), by the Danish Research Foundation, and under the European Union’s H2020 ERC Advanced Grant “Black holes: gravitational engines of discovery” grant agreement no. Gravitas–101052587. X.X. is supported by Deutsche Forschungsgemeinschaft under Germany’s Excellence Strategy EXC2121 “Quantum Universe” - 390833306. Views and opinions expressed are however those of the author only and do not necessarily reflect those of the European Union or the European Research Council. Neither the European Union nor the granting authority can be held responsible for them. This work was supported by FCT (Fundação para a Ciência e Tecnologia I.P, Portugal) under project No. 2022.01324.PTDC. This project has received funding from the European Union’s Horizon 2020 research and innovation programme under the Marie Skłodowska-Curie grant agreement No 101007855.

References

- [1] John Preskill, Mark B. Wise, and Frank Wilczek. Cosmology of the Invisible Axion. *Phys. Lett.*, 120B:127–132, 1983.
- [2] L. F. Abbott and P. Sikivie. A Cosmological Bound on the Invisible Axion. *Phys. Lett. B*, 120:133–136, 1983.
- [3] Michael Dine and Willy Fischler. The Not So Harmless Axion. *Phys. Lett. B*, 120:137–141, 1983.
- [4] Peter Svrcek and Edward Witten. Axions In String Theory. *JHEP*, 06:051, 2006.
- [5] S. A. Abel, M. D. Goodsell, J. Jaeckel, V. V. Khoze, and A. Ringwald. Kinetic Mixing of the Photon with Hidden U(1)s in String Phenomenology. *JHEP*, 07:124, 2008.
- [6] Asimina Arvanitaki, Savvas Dimopoulos, Sergei Dubovsky, Nemanja Kaloper, and John March-Russell. String Axiverse. *Phys. Rev.*, D81:123530, 2010.
- [7] Mark Goodsell, Joerg Jaeckel, Javier Redondo, and Andreas Ringwald. Naturally Light Hidden Photons in LARGE Volume String Compactifications. *JHEP*, 11:027, 2009.
- [8] Wayne Hu, Rennan Barkana, and Andrei Gruzinov. Cold and fuzzy dark matter. *Phys. Rev. Lett.*, 85:1158–1161, 2000.
- [9] R. Penrose and R. M. Floyd. Extraction of rotational energy from a black hole. *Nature*, 229:177–179, 1971.

- [10] Ya. B. Zel'Dovich. Generation of Waves by a Rotating Body. *Soviet Journal of Experimental and Theoretical Physics Letters*, 14:180, August 1971.
- [11] Steven L. Detweiler. KLEIN-GORDON EQUATION AND ROTATING BLACK HOLES. *Phys. Rev. D*, 22:2323–2326, 1980.
- [12] Vitor Cardoso and Shijun Yoshida. Superradiant instabilities of rotating black branes and strings. *JHEP*, 07:009, 2005.
- [13] Sam R. Dolan. Instability of the massive Klein-Gordon field on the Kerr spacetime. *Phys. Rev. D*, 76:084001, 2007.
- [14] Richard Brito, Vitor Cardoso, and Paolo Pani. Superradiance: New Frontiers in Black Hole Physics. *Lect. Notes Phys.*, 906:pp.1–237, 2015.
- [15] Richard Brito, Vitor Cardoso, and Paolo Pani. Black holes as particle detectors: evolution of superradiant instabilities. *Class. Quant. Grav.*, 32(13):134001, 2015.
- [16] William E. East and Frans Pretorius. Superradiant Instability and Backreaction of Massive Vector Fields around Kerr Black Holes. *Phys. Rev. Lett.*, 119(4):041101, 2017.
- [17] Carlos A. R. Herdeiro, Eugen Radu, and Nuno M. Santos. A bound on energy extraction (and hairiness) from superradiance. *Phys. Lett. B*, 824:136835, 2022.
- [18] Yifan Chen, Xiao Xue, Richard Brito, and Vitor Cardoso. Photon Ring Astrometry for Superradiant Clouds. *Phys. Rev. Lett.*, 130(11):111401, 2023.
- [19] Asimina Arvanitaki and Sergei Dubovsky. Exploring the String Axiverse with Precision Black Hole Physics. *Phys. Rev.*, D83:044026, 2011.
- [20] Asimina Arvanitaki, Masha Baryakhtar, and Xinlu Huang. Discovering the QCD Axion with Black Holes and Gravitational Waves. *Phys. Rev.*, D91(8):084011, 2015.
- [21] Masha Baryakhtar, Robert Lasenby, and Mae Teo. Black Hole Superradiance Signatures of Ultralight Vectors. *Phys. Rev. D*, 96(3):035019, 2017.
- [22] Richard Brito, Shrobona Ghosh, Enrico Barausse, Emanuele Berti, Vitor Cardoso, Irina Dvorkin, Antoine Klein, and Paolo Pani. Gravitational wave searches for ultralight bosons with LIGO and LISA. *Phys. Rev. D*, 96(6):064050, 2017.
- [23] Vitor Cardoso, Óscar J. C. Dias, Gavin S. Hartnett, Matthew Middleton, Paolo Pani, and Jorge E. Santos. Constraining the mass of dark photons and axion-like particles through black-hole superradiance. *JCAP*, 03:043, 2018.
- [24] Hooman Davoudiasl and Peter B Denton. Ultralight Boson Dark Matter and Event Horizon Telescope Observations of M87*. *Phys. Rev. Lett.*, 123(2):021102, 2019.
- [25] Richard Brito, Sara Grillo, and Paolo Pani. Black Hole Superradiant Instability from Ultralight Spin-2 Fields. *Phys. Rev. Lett.*, 124(21):211101, 2020.
- [26] Matthew J. Stott. Ultralight Bosonic Field Mass Bounds from Astrophysical Black Hole Spin. 9 2020.
- [27] Caner Ünal, Fabio Pacucci, and Abraham Loeb. Properties of ultralight bosons from heavy quasar spins via superradiance. *JCAP*, 05:007, 2021.
- [28] Akash Kumar Saha, Priyank Parashari, Tarak Nath Maity, Abhishek Dubey, Subhadip Bouri, and Ranjan Laha. Bounds on ultralight bosons from the Event Horizon Telescope observation of Sgr A*. 8 2022.
- [29] Hirotaka Yoshino and Hideo Kodama. Bosenova collapse of axion cloud around a rotating black hole. *Prog. Theor. Phys.*, 128:153–190, 2012.
- [30] Hirotaka Yoshino and Hideo Kodama. Gravitational radiation from an axion cloud around a black hole: Superradiant phase. *PTEP*, 2014:043E02, 2014.

- [31] Hirotaka Yoshino and Hideo Kodama. The bosonova and axiverse. *Class. Quant. Grav.*, 32(21):214001, 2015.
- [32] Richard Brito, Shrobona Ghosh, Enrico Barausse, Emanuele Berti, Vitor Cardoso, Irina Dvorkin, Antoine Klein, and Paolo Pani. Stochastic and resolvable gravitational waves from ultralight bosons. *Phys. Rev. Lett.*, 119(13):131101, 2017.
- [33] Maximiliano Isi, Ling Sun, Richard Brito, and Andrew Melatos. Directed searches for gravitational waves from ultralight bosons. *Phys. Rev. D*, 99(8):084042, 2019. [Erratum: *Phys.Rev.D* 102, 049901 (2020)].
- [34] Nils Siemonsen and William E. East. Gravitational wave signatures of ultralight vector bosons from black hole superradiance. *Phys. Rev. D*, 101(2):024019, 2020.
- [35] Ling Sun, Richard Brito, and Maximiliano Isi. Search for ultralight bosons in Cygnus X-1 with Advanced LIGO. *Phys. Rev. D*, 101(6):063020, 2020. [Erratum: *Phys.Rev.D* 102, 089902 (2020)].
- [36] Cristiano Palomba et al. Direct constraints on ultra-light boson mass from searches for continuous gravitational waves. *Phys. Rev. Lett.*, 123:171101, 2019.
- [37] Sylvia J. Zhu, Masha Baryakhtar, Maria Alessandra Papa, Daichi Tsuna, Norita Kawanaka, and Heinz-Bernd Eggenstein. Characterizing the continuous gravitational-wave signal from boson clouds around Galactic isolated black holes. *Phys. Rev. D*, 102(6):063020, 2020.
- [38] Leo Tsukada, Richard Brito, William E. East, and Nils Siemonsen. Modeling and searching for a stochastic gravitational-wave background from ultralight vector bosons. *Phys. Rev. D*, 103(8):083005, 2021.
- [39] Chen Yuan, Richard Brito, and Vitor Cardoso. Probing ultralight dark matter with future ground-based gravitational-wave detectors. *Phys. Rev. D*, 104(4):044011, 2021.
- [40] R. Abbott et al. All-sky search for gravitational wave emission from scalar boson clouds around spinning black holes in LIGO O3 data. *Phys. Rev. D*, 105(10):102001, 2022.
- [41] Chen Yuan, Yang Jiang, and Qing-Guo Huang. Constraints on an ultralight scalar boson from Advanced LIGO and Advanced Virgo’s first three observing runs using the stochastic gravitational-wave background. *Phys. Rev. D*, 106(2):023020, 2022.
- [42] Richard Brito and Shreya Shah. Extreme mass-ratio inspirals into black holes surrounded by scalar clouds. *Phys. Rev. D*, 108(8):084019, 2023.
- [43] Yifan Chen, Jing Shu, Xiao Xue, Qiang Yuan, and Yue Zhao. Probing Axions with Event Horizon Telescope Polarimetric Measurements. *Phys. Rev. Lett.*, 124(6):061102, 2020.
- [44] Guan-Wen Yuan, Zi-Qing Xia, Chengfeng Tang, Yaqi Zhao, Yi-Fu Cai, Yifan Chen, Jing Shu, and Qiang Yuan. Testing the ALP-photon coupling with polarization measurements of Sagittarius A*. *JCAP*, 03:018, 2021.
- [45] Yifan Chen, Yuxin Liu, Ru-Sen Lu, Yosuke Mizuno, Jing Shu, Xiao Xue, Qiang Yuan, and Yue Zhao. Stringent axion constraints with Event Horizon Telescope polarimetric measurements of M87*. *Nature Astron.*, 6(5):592–598, 2022.
- [46] Yifan Chen, Chunlong Li, Yosuke Mizuno, Jing Shu, Xiao Xue, Qiang Yuan, Yue Zhao, and Zihan Zhou. Birefringence tomography for axion cloud. *JCAP*, 09:073, 2022.
- [47] Andrei Gruzinov. Black Hole Spindown by Light Bosons. 4 2016.
- [48] Hajime Fukuda and Kazunori Nakayama. Aspects of Nonlinear Effect on Black Hole Superradiance. *JHEP*, 01:128, 2020.
- [49] Masha Baryakhtar, Marios Galanis, Robert Lasenby, and Olivier Simon. Black hole superradiance of self-interacting scalar fields. *Phys. Rev. D*, 103(9):095019, 2021.

- [50] Hidetoshi Omiya, Takuya Takahashi, and Takahiro Tanaka. Renormalization group analysis of superradiant growth of self-interacting axion cloud. *PTEP*, 2021(4):043E02, 2021.
- [51] Hidetoshi Omiya, Takuya Takahashi, and Takahiro Tanaka. Adiabatic evolution of the self-interacting axion field around rotating black holes. *PTEP*, 2022(4):043E03, 2022.
- [52] Hidetoshi Omiya, Takuya Takahashi, Takahiro Tanaka, and Hirotaka Yoshino. Impact of multiple modes on the evolution of self-interacting axion condensate around rotating black holes. *JCAP*, 06:016, 2023.
- [53] Spencer Collaviti, Ling Sun, Marios Galanis, and Masha Baryakhtar. Observational prospects of self-interacting scalar superradiance with next-generation gravitational-wave detectors. 7 2024.
- [54] Takuya Takahashi, Hidetoshi Omiya, and Takahiro Tanaka. Self-interacting axion clouds around rotating black holes in binary systems. *Phys. Rev. D*, 110(10):104038, 2024.
- [55] Josu C. Aurrekoetxea, James Marsden, Katy Clough, and Pedro G. Ferreira. Self-interacting scalar dark matter around binary black holes. *Phys. Rev. D*, 110(8):083011, 2024.
- [56] João G. Rosa and Thomas W. Kephart. Stimulated Axion Decay in Superradiant Clouds around Primordial Black Holes. *Phys. Rev. Lett.*, 120(23):231102, 2018.
- [57] Mateja Boskovic, Richard Brito, Vitor Cardoso, Taishi Ikeda, and Helvi Witek. Axionic instabilities and new black hole solutions. *Phys. Rev. D*, 99(3):035006, 2019.
- [58] Taishi Ikeda, Richard Brito, and Vitor Cardoso. Blasts of Light from Axions. *Phys. Rev. Lett.*, 122(8):081101, 2019.
- [59] Thomas F. M. Spieksma, Enrico Cannizzaro, Taishi Ikeda, Vitor Cardoso, and Yifan Chen. Superradiance: Axionic couplings and plasma effects. *Phys. Rev. D*, 108(6):063013, 2023.
- [60] Patrick B. Greene and Lev Kofman. Preheating of fermions. *Phys. Lett. B*, 448:6–12, 1999.
- [61] Patrick B. Greene and Lev Kofman. On the theory of fermionic preheating. *Phys. Rev. D*, 62:123516, 2000.
- [62] Julian S. Schwinger. On gauge invariance and vacuum polarization. *Phys. Rev.*, 82:664–679, 1951.
- [63] Francesco D’Eramo and Jesse Thaler. Semi-annihilation of Dark Matter. *JHEP*, 06:109, 2010.
- [64] Junwu Huang and Yue Zhao. Dark Matter Induced Nucleon Decay: Model and Signatures. *JHEP*, 02:077, 2014.
- [65] Kaustubh Agashe, Yanou Cui, Lina Necib, and Jesse Thaler. (In)direct Detection of Boosted Dark Matter. *JCAP*, 10:062, 2014.
- [66] Joachim Kopp, Jia Liu, and Xiao-Ping Wang. Boosted Dark Matter in IceCube and at the Galactic Center. *JHEP*, 04:105, 2015.
- [67] Atri Bhattacharya, Raj Gandhi, Aritra Gupta, and Satyanarayan Mukhopadhyay. Boosted Dark Matter and its implications for the features in IceCube HESE data. *JCAP*, 05:002, 2017.
- [68] Ayuki Kamada, Hee Jung Kim, Hyungjin Kim, and Toyokazu Sekiguchi. Self-Heating Dark Matter via Semiannihilation. *Phys. Rev. Lett.*, 120(13):131802, 2018.
- [69] C. Kachulis et al. Search for Boosted Dark Matter Interacting With Electrons in Super-Kamiokande. *Phys. Rev. Lett.*, 120(22):221301, 2018.
- [70] Animesh Chatterjee, Albert De Roeck, Doojin Kim, Zahra Gh. Moghaddam, Jong-Chul Park, Seodong Shin, Leigh H. Whitehead, and Jaehoon Yu. Searching for boosted dark matter at ProtoDUNE. *Phys. Rev. D*, 98(7):075027, 2018.
- [71] Ayuki Kamada, Hee Jung Kim, and Hyungjin Kim. Self-heating of Strongly Interacting Massive Particles. *Phys. Rev. D*, 98(2):023509, 2018.

- [72] David McKeen and Nirmal Raj. Monochromatic dark neutrinos and boosted dark matter in noble liquid direct detection. *Phys. Rev. D*, 99(10):103003, 2019.
- [73] C. A. Argüelles et al. New opportunities at the next-generation neutrino experiments I: BSM neutrino physics and dark matter. *Rept. Prog. Phys.*, 83(12):124201, 2020.
- [74] Ayuki Kamada and Hee Jung Kim. Escalating core formation with dark matter self-heating. *Phys. Rev. D*, 102(4):043009, 2020.
- [75] Joshua Berger, Yanou Cui, Mathew Graham, Lina Necib, Gianluca Petrillo, Dane Stocks, Yun-Tse Tsai, and Yue Zhao. Prospects for detecting boosted dark matter in DUNE through hadronic interactions. *Phys. Rev. D*, 103(9):095012, 2021.
- [76] Babak Abi et al. Deep Underground Neutrino Experiment (DUNE), Far Detector Technical Design Report, Volume II: DUNE Physics. 2 2020.
- [77] G. B. Gelmini and M. Roncadelli. Left-Handed Neutrino Mass Scale and Spontaneously Broken Lepton Number. *Phys. Lett. B*, 99:411–415, 1981.
- [78] H. Georgi and S. L. Glashow. Unity of All Elementary Particle Forces. *Phys. Rev. Lett.*, 32:438–441, 1974.
- [79] Jogesh C. Pati and Abdus Salam. Lepton Number as the Fourth Color. *Phys. Rev. D*, 10:275–289, 1974. [Erratum: *Phys.Rev.D* 11, 703–703 (1975)].
- [80] Rabindra N. Mohapatra and Jogesh C. Pati. Left-Right Gauge Symmetry and an Isoconjugate Model of CP Violation. *Phys. Rev. D*, 11:566–571, 1975.
- [81] Jeffrey M. Berryman et al. Neutrino Self-Interactions: A White Paper. In *Snowmass 2021*, 3 2022.
- [82] Edoardo Vitagliano, Irene Tamborra, and Georg Raffelt. Grand Unified Neutrino Spectrum at Earth: Sources and Spectral Components. *Rev. Mod. Phys.*, 92:45006, 2020.
- [83] Ann E. Nelson and Jakub Scholtz. Dark Light, Dark Matter and the Misalignment Mechanism. *Phys. Rev. D*, 84:103501, 2011.
- [84] Nils Siemonsen, Cristina Mondino, Daniel Egana-Ugrinovic, Junwu Huang, Masha Baryakhtar, and William E. East. Dark photon superradiance: Electrodynamics and multimessenger signals. *Phys. Rev. D*, 107(7):075025, 2023.
- [85] Diego Blas and Samuel J. Witte. Quenching Mechanisms of Photon Superradiance. *Phys. Rev. D*, 102(12):123018, 2020.
- [86] Ya. B. Zeldovich and Alexei A. Starobinsky. Particle production and vacuum polarization in an anisotropic gravitational field. *Zh. Eksp. Teor. Fiz.*, 61:2161–2175, 1971.
- [87] Lev Kofman, Andrei D. Linde, and Alexei A. Starobinsky. Towards the theory of reheating after inflation. *Phys. Rev. D*, 56:3258–3295, 1997.
- [88] Asher Berlin and Anson Hook. Searching for Millicharged Particles with Superconducting Radio-Frequency Cavities. *Phys. Rev. D*, 102(3):035010, 2020.
- [89] A.A. Grib, S.G. Mamayev, V.M. Mostepanenko, and V.M. Mostepanenko. *Vacuum Quantum Effects in Strong Fields*. Friedmann Laboratory Pub., 1994.
- [90] Thomas Erber. High-energy electromagnetic conversion processes in intense magnetic fields. *Rev. Mod. Phys.*, 38:626–659, 1966.
- [91] A. A. Sokolov and I. M. Ternov. *Synchrotron radiation*. 1966.
- [92] T. G. Blackburn. Radiation reaction in electron-beam interactions with high-intensity lasers. *Plasma Phys.*, 4:5, 2020.

- [93] Jean-Philippe Uzan, Martin Pernot-Borràs, and Joel Bergé. Effects of a scalar fifth force on the dynamics of a charged particle as a new experimental design to test chameleon theories. *Phys. Rev. D*, 102(4):044059, 2020.
- [94] George Casella, Christian Robert, and Martin Wells. Generalized accept-reject sampling schemes. *Lecture Notes-Monograph Series*, 45, 01 2004.
- [95] Abhish Dev, Gordan Krnjaic, Pedro Machado, and Harikrishnan Ramani. Constraining feeble neutrino interactions with ultralight dark matter. *Phys. Rev. D*, 107(3):035006, 2023.
- [96] W. Heisenberg and H. Euler. Consequences of Dirac’s theory of positrons. *Z. Phys.*, 98(11-12):714–732, 1936.
- [97] Peter W. Graham, David E. Kaplan, Jeremy Mardon, Surjeet Rajendran, and William A. Terrano. Dark Matter Direct Detection with Accelerometers. *Phys. Rev. D*, 93(7):075029, 2016.
- [98] Joel Bergé, Philippe Brax, Gilles Métris, Martin Pernot-Borràs, Pierre Touboul, and Jean-Philippe Uzan. MICROSCOPE Mission: First Constraints on the Violation of the Weak Equivalence Principle by a Light Scalar Dilaton. *Phys. Rev. Lett.*, 120(14):141101, 2018.
- [99] Aurélien Hees, Olivier Minazzoli, Etienne Savalle, Yevgeny V. Stadnik, and Peter Wolf. Violation of the equivalence principle from light scalar dark matter. *Phys. Rev. D*, 98(6):064051, 2018.
- [100] Aaron Pierce, Keith Riles, and Yue Zhao. Searching for Dark Photon Dark Matter with Gravitational Wave Detectors. *Phys. Rev. Lett.*, 121(6):061102, 2018.
- [101] Colin J. Kennedy, Eric Oelker, John M. Robinson, Tobias Bothwell, Dhruv Kedar, William R. Milner, G. Edward Marti, Andrei Derevianko, and Jun Ye. Precision Metrology Meets Cosmology: Improved Constraints on Ultralight Dark Matter from Atom-Cavity Frequency Comparisons. *Phys. Rev. Lett.*, 125(20):201302, 2020.
- [102] R. Abbott et al. Constraints on dark photon dark matter using data from LIGO’s and Virgo’s third observing run. *Phys. Rev. D*, 105(6):063030, 2022.
- [103] E. A. Shaw, M. P. Ross, C. A. Hagedorn, E. G. Adelberger, and J. H. Gundlach. Torsion-balance search for ultralow-mass bosonic dark matter. *Phys. Rev. D*, 105(4):042007, 2022.
- [104] Xiao Xue et al. High-precision search for dark photon dark matter with the Parkes Pulsar Timing Array. *Phys. Rev. Res.*, 4(1):L012022, 2022.
- [105] Shao-Feng Ge and Pedro Pasquini. Probing light mediators in the radiative emission of neutrino pair. *Eur. Phys. J. C*, 82(3):208, 2022.
- [106] Jiang-Chuan Yu, Yue-Hui Yao, Yong Tang, and Yue-Liang Wu. Sensitivity of space-based gravitational-wave interferometers to ultralight bosonic fields and dark matter. *Phys. Rev. D*, 108(8):083007, 2023.
- [107] Adeela Afzal et al. The NANOGrav 15 yr Data Set: Search for Signals from New Physics. *Astrophys. J. Lett.*, 951(1):L11, 2023. [Erratum: *Astrophys.J.Lett.* 971, L27 (2024), Erratum: *Astrophys.J.* 971, L27 (2024)].
- [108] Y. Chikashige, Rabindra N. Mohapatra, and R. D. Peccei. Are There Real Goldstone Bosons Associated with Broken Lepton Number? *Phys. Lett. B*, 98:265–268, 1981.
- [109] C. S. Aulakh and Rabindra N. Mohapatra. Neutrino as the Supersymmetric Partner of the Majoron. *Phys. Lett. B*, 119:136–140, 1982.
- [110] Harald Fritzsch and Peter Minkowski. Unified Interactions of Leptons and Hadrons. *Annals Phys.*, 93:193–266, 1975.
- [111] Howard Georgi. The State of the Art—Gauge Theories. *AIP Conf. Proc.*, 23:575–582, 1975.

- [112] Edward W. Kolb and Michael S. Turner. Supernova SN 1987a and the Secret Interactions of Neutrinos. *Phys. Rev. D*, 36:2895, 1987.
- [113] M. Kachelriess, R. Tomas, and J. W. F. Valle. Supernova bounds on Majoron emitting decays of light neutrinos. *Phys. Rev. D*, 62:023004, 2000.
- [114] Yasaman Farzan. Bounds on the coupling of the Majoron to light neutrinos from supernova cooling. *Phys. Rev. D*, 67:073015, 2003.
- [115] A. Gando et al. Limits on Majoron-emitting double-beta decays of Xe-136 in the KamLAND-Zen experiment. *Phys. Rev. C*, 86:021601, 2012.
- [116] Tim Brune and Heinrich Päs. Massive Majorons and constraints on the Majoron-neutrino coupling. *Phys. Rev. D*, 99(9):096005, 2019.
- [117] Guo-yuan Huang, Tommy Ohlsson, and Shun Zhou. Observational Constraints on Secret Neutrino Interactions from Big Bang Nucleosynthesis. *Phys. Rev. D*, 97(7):075009, 2018.
- [118] Francesco Forastieri, Massimiliano Lattanzi, and Paolo Natoli. Cosmological constraints on neutrino self-interactions with a light mediator. *Phys. Rev. D*, 100(10):103526, 2019.
- [119] Shao-Ping Li and Xun-Jie Xu. N_{eff} constraints on light mediators coupled to neutrinos: the dilution-resistant effect. *JHEP*, 10:012, 2023.
- [120] Miguel Escudero and Samuel J. Witte. A CMB search for the neutrino mass mechanism and its relation to the Hubble tension. *Eur. Phys. J. C*, 80(4):294, 2020.
- [121] Damiano F. G. Fiorillo, Georg G. Raffelt, and Edoardo Vitagliano. Strong Supernova 1987A Constraints on Bosons Decaying to Neutrinos. *Phys. Rev. Lett.*, 131(2):021001, 2023.
- [122] Stefan Sandner, Miguel Escudero, and Samuel J. Witte. Precision CMB constraints on eV-scale bosons coupled to neutrinos. *Eur. Phys. J. C*, 83(8):709, 2023.
- [123] Damiano F. G. Fiorillo, Georg G. Raffelt, and Edoardo Vitagliano. Supernova emission of secretly interacting neutrino fluid: Theoretical foundations. *Phys. Rev. D*, 109(2):023017, 2024.
- [124] Damiano F. G. Fiorillo, Georg G. Raffelt, and Edoardo Vitagliano. Large Neutrino Secret Interactions Have a Small Impact on Supernovae. *Phys. Rev. Lett.*, 132(2):021002, 2024.
- [125] Matías M. Reynoso and Oscar A. Sampayo. Propagation of high-energy neutrinos in a background of ultralight scalar dark matter. *Astropart. Phys.*, 82:10–20, 2016.
- [126] Asher Berlin. Neutrino Oscillations as a Probe of Light Scalar Dark Matter. *Phys. Rev. Lett.*, 117(23):231801, 2016.
- [127] Gordan Krnjaic, Pedro A. N. Machado, and Lina Necib. Distorted neutrino oscillations from time varying cosmic fields. *Phys. Rev. D*, 97(7):075017, 2018.
- [128] Vedran Brdar, Joachim Kopp, Jia Liu, Pascal Prass, and Xiao-Ping Wang. Fuzzy dark matter and nonstandard neutrino interactions. *Phys. Rev. D*, 97(4):043001, 2018.
- [129] Hooman Davoudiasl, Gopolang Mohlabeng, and Matthew Sullivan. Galactic Dark Matter Population as the Source of Neutrino Masses. *Phys. Rev. D*, 98(2):021301, 2018.
- [130] Jiajun Liao, Danny Marfatia, and Kerry Whisnant. Light scalar dark matter at neutrino oscillation experiments. *JHEP*, 04:136, 2018.
- [131] Francesco Capozzi, Ian M. Shoemaker, and Luca Vecchi. Neutrino Oscillations in Dark Backgrounds. *JCAP*, 07:004, 2018.
- [132] Guo-Yuan Huang and Newton Nath. Neutrinophilic Axion-Like Dark Matter. *Eur. Phys. J. C*, 78(11):922, 2018.
- [133] Yasaman Farzan. Ultra-light scalar saving the $3 + 1$ neutrino scheme from the cosmological bounds. *Phys. Lett. B*, 797:134911, 2019.

- [134] James M. Cline. Viable secret neutrino interactions with ultralight dark matter. *Phys. Lett. B*, 802:135182, 2020.
- [135] Abhish Dev, Pedro A. N. Machado, and Pablo Martínez-Miravé. Signatures of ultralight dark matter in neutrino oscillation experiments. *JHEP*, 01:094, 2021.
- [136] Marta Losada, Yosef Nir, Gilad Perez, and Yogev Shpilman. Probing scalar dark matter oscillations with neutrino oscillations. *JHEP*, 04:030, 2022.
- [137] Guo-yuan Huang and Newton Nath. Neutrino meets ultralight dark matter: $0\nu\beta\beta$ decay and cosmology. *JCAP*, 05(05):034, 2022.
- [138] Eung Jin Chun. Neutrino Transition in Dark Matter. 12 2021.
- [139] Guo-yuan Huang, Manfred Lindner, Pablo Martínez-Miravé, and Manibrata Sen. Cosmology-friendly time-varying neutrino masses via the sterile neutrino portal. *Phys. Rev. D*, 106(3):033004, 2022.
- [140] Marta Losada, Yosef Nir, Gilad Perez, Inbar Savoray, and Yogev Shpilman. Parametric resonance in neutrino oscillations induced by ultra-light dark matter and implications for KamLAND and JUNO. *JHEP*, 03:032, 2023.
- [141] Dawid Brzeminski, Saurav Das, Anson Hook, and Clayton Ristow. Constraining Vector Dark Matter with neutrino experiments. *JHEP*, 08:181, 2023.
- [142] Gonzalo Alonso-Álvarez, Katarina Bleau, and James M. Cline. Distortion of neutrino oscillations by dark photon dark matter. *Phys. Rev. D*, 107(5):055045, 2023.
- [143] YeolLin ChoeJo, Yechan Kim, and Hye-Sung Lee. Dirac-Majorana neutrino type oscillation induced by a wave dark matter. *Phys. Rev. D*, 108(9):095028, 2023.
- [144] Marta Losada, Yosef Nir, Gilad Perez, Inbar Savoray, and Yogev Shpilman. Time dependent CP-even and CP-odd signatures of scalar ultralight dark matter in neutrino oscillations. *Phys. Rev. D*, 108(5):055004, 2023.
- [145] Ranjan Laha, Basudeb Dasgupta, and John F. Beacom. Constraints on New Neutrino Interactions via Light Abelian Vector Bosons. *Phys. Rev. D*, 89(9):093025, 2014.
- [146] Pouya Bakhti and Yasaman Farzan. Constraining secret gauge interactions of neutrinos by meson decays. *Phys. Rev. D*, 95(9):095008, 2017.
- [147] Miguel Escudero, Dan Hooper, Gordan Krnjaic, and Mathias Pierre. Cosmology with A Very Light $L_\mu - L_\tau$ Gauge Boson. *JHEP*, 03:071, 2019.
- [148] Majid Bahrminasr, Pouya Bakhti, and Meshkat Rajaei. Sensitivities to secret neutrino interaction at FASER ν . *J. Phys. G*, 48(9):095001, 2021.
- [149] Jeff A. Dror. Discovering leptonic forces using nonconserved currents. *Phys. Rev. D*, 101(9):095013, 2020.
- [150] Majid Ekhterachian, Anson Hook, Soubhik Kumar, and Yuhsin Tsai. Bounds on gauge bosons coupled to nonconserved currents. *Phys. Rev. D*, 104(3):035034, 2021.
- [151] Masoom Singh, Mauricio Bustamante, and Sanjib Kumar Agarwalla. Flavor-dependent long-range neutrino interactions in DUNE & T2HK: alone they constrain, together they discover. *JHEP*, 08:101, 2023.
- [152] N. Aghanim et al. Planck 2018 results. VI. Cosmological parameters. *Astron. Astrophys.*, 641:A6, 2020. [Erratum: *Astron. Astrophys.* 652, C4 (2021)].
- [153] Patrick Stöcker et al. Strengthening the bound on the mass of the lightest neutrino with terrestrial and cosmological experiments. *Phys. Rev. D*, 103(12):123508, 2021.
- [154] Walter H. G. Lewin, Jan van Paradijs, and Edward Peter Jacobus van den Heuvel. *X-ray Binaries*. 1997.

- [155] Shude Mao, Martin C. Smith, P. Wozniak, A. Udalski, M. Szymanski M. Kubiak, G. Pietrzynski, I. Soszynski, and K. Zebrun. Optical gravitational lensing experiment. ogle-1999-bul-32: the longest ever microlensing event - evidence for a stellar mass black hole? *Mon. Not. Roy. Astron. Soc.*, 329:349, 2002.
- [156] D. P. Bennett et al. Gravitational microlensing events due to stellar mass black holes. *Astrophys. J.*, 579:639–659, 2002.
- [157] Leor Barack et al. Black holes, gravitational waves and fundamental physics: a roadmap. *Class. Quant. Grav.*, 36(14):143001, 2019.
- [158] Laura W. Brenneman and Christopher S. Reynolds. Constraining Black Hole Spin Via X-ray Spectroscopy. *Astrophys. J.*, 652:1028–1043, 2006.
- [159] Kazunori Akiyama et al. First M87 Event Horizon Telescope Results. I. The Shadow of the Supermassive Black Hole. *Astrophys. J. Lett.*, 875:L1, 2019.
- [160] Kazunori Akiyama et al. First Sagittarius A* Event Horizon Telescope Results. I. The Shadow of the Supermassive Black Hole in the Center of the Milky Way. *Astrophys. J. Lett.*, 930(2):L12, 2022.
- [161] M. G. Aartsen et al. Search for steady point-like sources in the astrophysical muon neutrino flux with 8 years of IceCube data. *Eur. Phys. J. C*, 79(3):234, 2019.
- [162] R. Abbasi et al. Observation of high-energy neutrinos from the Galactic plane. *Science*, 380:6652, 7 2023.
- [163] Shao-Feng Ge, Jianglai Liu, Qiang Yuan, and Ning Zhou. Diurnal Effect of Sub-GeV Dark Matter Boosted by Cosmic Rays. *Phys. Rev. Lett.*, 126(9):091804, 2021.
- [164] Bartosz Fornal, Pearl Sandick, Jing Shu, Meng Su, and Yue Zhao. Boosted Dark Matter Interpretation of the XENON1T Excess. *Phys. Rev. Lett.*, 125(16):161804, 2020.
- [165] Yifan Chen, Bartosz Fornal, Pearl Sandick, Jing Shu, Xiao Xue, Yue Zhao, and Junchao Zong. Earth shielding and daily modulation from electrophilic boosted dark particles. *Phys. Rev. D*, 107(3):033006, 2023.
- [166] Chen Xia, Yan-Hao Xu, and Yu-Feng Zhou. Production and attenuation of cosmic-ray boosted dark matter. *JCAP*, 02(02):028, 2022.
- [167] Xiangyi Cui et al. Search for Cosmic-Ray Boosted Sub-GeV Dark Matter at the PandaX-II Experiment. *Phys. Rev. Lett.*, 128(17):171801, 2022.
- [168] Mai Qiao, Chen Xia, and Yu-Feng Zhou. Diurnal modulation of electron recoils from DM-nucleon scattering through the Migdal effect. *JCAP*, 11:079, 2023.
- [169] Sven E. Vahsen, Ciaran A. J. O’Hare, and Dinesh Loomba. Directional Recoil Detection. *Ann. Rev. Nucl. Part. Sci.*, 71:189–224, 2021.
- [170] M. G. Aartsen et al. Measurement of the Atmospheric ν_e Spectrum with IceCube. *Phys. Rev. D*, 91:122004, 2015.
- [171] E. Richard et al. Measurements of the atmospheric neutrino flux by Super-Kamiokande: energy spectra, geomagnetic effects, and solar modulation. *Phys. Rev. D*, 94(5):052001, 2016.
- [172] A. Albert et al. All-flavor Search for a Diffuse Flux of Cosmic Neutrinos with Nine Years of ANTARES Data. *Astrophys. J. Lett.*, 853(1):L7, 2018.
- [173] V. A. Allakhverdyan et al. Diffuse neutrino flux measurements with the Baikal-GVD neutrino telescope. *Phys. Rev. D*, 107(4):042005, 2023.
- [174] Giulia Illuminati and Sergio Alves. Searches for Point-like Sources of Cosmic Neutrinos with 15 Years of ANTARES Data. *PoS, ICRC2023:1128*, 2023.

- [175] V. M. Aynutdinov et al. Track-like event analysis at the Baikal-GVD neutrino telescope. *PoS*, ICRC2023:1001, 2023.
- [176] S. Adrian-Martinez et al. Letter of intent for KM3NeT 2.0. *J. Phys. G*, 43(8):084001, 2016.
- [177] Matteo Agostini et al. The Pacific Ocean Neutrino Experiment. *Nature Astron.*, 4(10):913–915, 2020.
- [178] M. G. Aartsen et al. IceCube-Gen2: the window to the extreme Universe. *J. Phys. G*, 48(6):060501, 2021.
- [179] Z. P. Ye et al. A multi-cubic-kilometre neutrino telescope in the western pacific ocean. *Nature Astronomy*, 7(12):1497–1505, 2023.
- [180] M. G. Aartsen et al. Energy Reconstruction Methods in the IceCube Neutrino Telescope. *JINST*, 9:P03009, 2014.
- [181] S. Aiello et al. Sensitivity of the KM3NeT/ARCA neutrino telescope to point-like neutrino sources. *Astropart. Phys.*, 111:100–110, 2019.
- [182] Damiano F. G. Fiorillo, Mauricio Bustamante, and Victor B. Valera. Near-future discovery of point sources of ultra-high-energy neutrinos. *JCAP*, 03:026, 2023.
- [183] Lisa Johanna Schumacher, Matthias Huber, Matteo Agostini, Mauricio Bustamante, Foteini Oikonomou, and Elisa Resconi. PLE ν M: A global and distributed monitoring system of high-energy astrophysical neutrinos. *PoS*, ICRC2021:1185, 2021.